JM PAPERS

Numerical analysis of flow and stress redistribution at an open-to-closed channel transition caused by floating debris carpets

Chit Yan Toe[1] , **Wim Uijttewaal**[1] , **Baptiste Hardy**[2] , **Akshay Patil**[3] , **Pedro Costa**[2] and **Davide Wüthrich**[1]

[1]Department of Hydraulic Engineering, Faculty of Civil Engineering and Geosciences, Delft University of Technology, Delft, The Netherlands

[2]Department of Process & Energy, Faculty of Mechanical Engineering, Delft University of Technology, Delft, The Netherlands

[3]3D Geoinformation Research Group, Department of Urbanism, Faculty of Architecture and the Built Environment, Delft University of Technology, Delft, The Netherlands

Corresponding author: Chit Yan Toe, c.yantoe-1@tudelft.nl

This research investigates the hydrodynamics of a physical boundary transition from free slip to no slip, which usually occurs in ice-jams, large wood and debris accumulation in free-surface flows. Using direct numerical simulation coupled with a volume penalisation method, a series of numerical simulations is performed for an open-channel flow covered with a layer of floating spherical particles, replicating the laboratory set-up of Yan Toe *et al.* (2025 *J. Hydraul. Eng.*, vol. 151, 04025010). Flow transition from the open channel to the closed channel induces a new boundary-layer development at the top surface, accompanied by a flow separation and an increased bottom shear stress that enhances particle mobility at the bottom. Analysis of a fully developed flow in an asymmetric roughness channel (rough surface at the top boundary and smooth surface at the bottom boundary) also shows that the vertical position of maximum velocity is higher than the position of zero Reynolds shear stress, which supports the experimental observation of Hanjalić & Launder (*J. Fluid Mech.*, vol. 51, 1972, pp. 301–335), demonstrating the shortcoming of traditional turbulence closure models such as the $k-\varepsilon$ model. Finally, the stagnation force acting on a particle at the leading edge of the accumulation layer is compared with the analytical prediction of Yan Toe *et al.* Understanding the flow transition

improves the prediction of the stability threshold of the accumulation layer and design criteria for debris-collection devices.

Key words: particle/fluid flows, turbulent boundary layers, hydraulics

1. Introduction

Fluvial systems undergo systematic changes in their hydrodynamic response due to ice-jams, logjams at racks and debris accumulation at waste-collection devices (to list a few) as shown in figure 1. In such cases, accumulation of floating materials can induce a transition from a free-surface flow condition to closed-channel-like flow, resulting in complex flow behaviour such as Kelvin–Helmholtz instability and flow separation that depends on the roughness characteristics of the debris at the free surface (Fang, Tachie & Dow 2022). Such a change in the boundary condition at the top boundary significantly alters the hydrodynamic response in both the upstream and downstream reaches of the flow domain (Saito & Pullin 2014; Ismail, Zaki & Durbin 2018). Specifically, in the vicinity of the transition, the flow encounters significant changes in the mean velocity profile, shear stress and acceleration that can lead to increased turbulent transport, erosion at the bottom boundary and increased instability of the accumulation layer. As a result, understanding the physics of such a flow transition due to the accumulation layer can provide crucial insights to accurately predict its stability and better design hydraulic structures that can efficiently capture floating debris.

Focusing on the formation of a layer of floating material, called a carpet, its life cycle can be divided into the following stages: (i) initiation of accumulation due to the presence of hydraulic structures, (ii) progression due to incoming debris, (iii) stabilisation of the carpet and (iv) mechanical breakup or instability due to unbalanced forces. Depending on the type of debris transported by the incoming flow, carpet formation may consist of one or more layers over the depth of the channel (Shen 2010; Schalko *et al.* 2018; Yan Toe *et al.* 2025). Additionally, surface roughness characteristics of the carpet can differ greatly from those of the channel bed, leading to an asymmetric shear stress distribution as sketched in the downstream reach of the carpet in figure 1. This is typically observed in ice-jams and debris accumulation in rivers (Tatinclaux & Gogus 1983; Jueyi *et al.* 2010; Luo *et al.* 2025). Moreover, river morphology is greatly influenced by the surface roughness of ice cover, implying that a larger ratio of ice-cover roughness to bed roughness enhances riverbed erosion (Luo *et al.* 2025). Moreover, there is still a debate as to whether the location of maximum velocity coincides with the location of zero shear stress in asymmetric channel flows. Hanjalić & Launder (1972), Tatinclaux & Gogus (1983) and Parthasarathy & Muste (1994) confirmed through experimental data that the two locations are not identical. In contrast, Shen & Harden (1978), Guo *et al.* (2017) and Huai *et al.* (2024) assumed these locations to coincide in their analyses, leading to the development of two distinct schools of thought. Thus, the momentum flux across the point of zero mean strain ($\partial \overline{u}_1 / \partial x_3 = 0$; see figure 1) still remains poorly understood for such a hydraulic system. Therefore, the asymmetry in wall roughness conditions imposes further challenges in correctly estimating the friction coefficients of the boundaries of such hydraulic systems, which are also susceptible to destabilising hydrodynamic forces (Hanjalić & Launder 1972; Guo *et al.* 2017; Yan Toe *et al.* 2025).

As for the stability of the carpet, the hydrodynamic forces acting on the debris and interparticle forces determine the threshold mobility, and consequently the overall stability
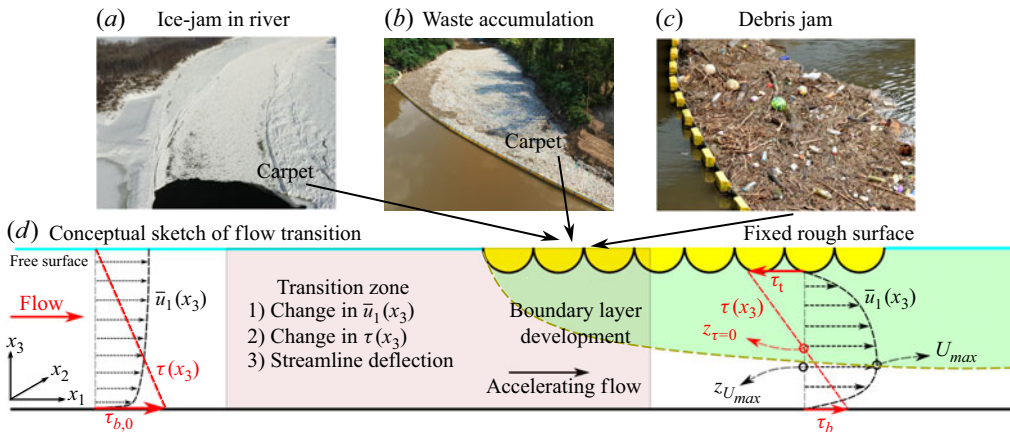
Figure 1. Flow transitions from open channel to closed channel. (*a*) Ice-jam in a river (photo: Bryan Hopkins). (*b*) Plastic waste accumulation upstream of a waste-collection device (photo: The Ocean Cleanup). (*c*) Debris jam (Copyright Albert Bridge (image reused under CC Attribution-Sharealike)). (*d*) Schematic of the flow transition from an open channel to a closed channel (not to scale), based on Yan Toe, Uijttewaal & Wüthrich (2025).

of the carpet. For plastic particles, the hydrodynamic forces affect substantially the global stability of the carpet due to a lack of interparticle cohesion, thus making them susceptible to various instability mechanisms as detailed in Yan Toe *et al.* (2025). For the ice carpets often observed in ice-jams, Beltaos (1983), Zufelt & Ettema (2000) and Shen, Liu & Chen (2001) developed mathematical models to predict the carpet thickness under the static and dynamic flow conditions, assuming a continuum model for ice. Differently from the continuum assumption, Jueyi *et al.* (2010) experimentally investigated incipient motion of individual ice particles under cover and provided a stability criterion, similar to the Shields criterion used in sediment transport. Unlike ice-jams, plastic debris does not interact thermally or through mass transfer (i.e. ice melting), but primarily through hydrodynamic interactions with the carrier phase (i.e. water). Therefore, mechanical properties of the particles and flow conditions are mainly considered in the stability of plastic debris accumulation. In addition to the particle transport at the leading edge of the carpet (called erosion), particles inside the carpet can be squeezed out vertically due to the cumulative compressive force along the carpet (called squeezing), which is similar to the buckling phenomenon observed by Tordesillas & Muthuswamy (2009) in force chains. To that end, Yan Toe *et al.* (2025) developed and validated analytical formulae of these two instability modes, based on the mean flow velocity, particle diameter and particle density in an idealised single-layer carpet of mono-dispersed spherical plastic particles.

For the squeezing instability, a proper estimate of the cumulative shear stress is required to estimate the destabilising force acting on a particle. Since the flow transitions from an open channel flow to a closed channel with varying hydraulic roughness, estimation of shear stress is non-trivial, especially in the transition region. On this front, Li *et al.* (2019) and Rouhi, Chung & Hutchins (2019) studied a turbulent boundary layer with roughness transition, and Van Buren *et al.* (2020) studied a turbulent pipe flow with a similar transition, proving that adjustment of turbulent stresses requires a longer downstream fetch than the development length required for the mean flow recovery.

Although there is a substantial literature discussing the boundary-layer development subject to a rough–smooth transition (Antonia & Luxton 1971; Van Buren *et al.* 2020),

C. Yan Toe, W. Uijttewaal, B. Hardy, A. Patil, P. Costa and D. Wüthrich

the hydrodynamics subject to free slip (open channel) to no slip (closed channel) at the top boundary has not been extensively explored. This is particularly interesting as the boundary layers at the smooth bottom and the rough top interact in the downstream fetch of the carpet, leading to a peculiar flow response in the vicinity of the transition. Adding to the complexity, different roughnesses at the top and bottom boundaries further complicate the momentum mixing and consequently it is more challenging to estimate the friction coefficients. These hydrodynamic interactions hinder the prediction of particle instability, irrespective of the material properties of the particle, i.e. sediment at the riverbed, or plastic particles at the floating carpet. Consequently, in this work, we aim to address the hydrodynamics of an idealised open-to-closed channel transition (figure 1), and its implications for the stability of mono-dispersed spherical particles inside a floating carpet.

To this end, three research questions are formulated as follows:

(i) How do the shear stresses and the friction coefficients develop along the bottom and top surfaces beyond the carpet transition?
(ii) What changes in the mean flow are observed near the transition?
(iii) What are the implications for erosion processes at the bottom boundary and particle instability of debris accumulation?

By better understanding the boundary-layer development at the transition, we aim to further improve the analytical formulations for particle instability, and subsequently better design waste-collection devices and improve river sediment management. It should be noted that the present study considers only mono-dispersed spherical particles as roughness elements, which differ from realistic debris that is more complex in composition, size and shape. For example, plastic waste with cylindrical or foil-like shapes is often found mixed with organic materials, complicating the characterisation of surface roughness. Similarly, large wood accumulations differ in size and shape from spherical elements, with their random orientations leading to a complex porosity within the accumulation layer. Therefore, the flow properties and streamlines, particularly the turbulent stresses near and within the accumulation layer, may differ between the simulation results and realistic configurations. Nevertheless, the present direct numerical simulation (DNS) study is expected to provide valuable insight about mean flow development and Reynolds stress profiles below a generic carpet of debris, waste or ice, and should serve as a baseline for future studies that would address the complex factors described above.

In the following sections, we first present the computational method and various flow configurations to answer the above-mentioned research questions. This is followed by a detailed discussion of the various hydrodynamic parameters of interest. Finally, we present concluding remarks and outline future work to support our analytical model.

2. Methods

The flow configurations investigated in this work are addressed using DNS of the Navier–Stokes equations, coupled with a volume penalisation method (Fadlun *et al.* 2000) to represent a rough carpet layer in the computational domain.

2.1. *Governing equations and numerical methods*

The differential forms of the incompressible Navier–Stokes momentum and mass conservation equations are considered in this work, given by

$$\frac{\partial u_i}{\partial t} + \frac{\partial u_i u_j}{\partial x_j} = -\frac{1}{\rho}\frac{\partial p}{\partial x_i} + \nu\frac{\partial^2 u_i}{\partial x_j \partial x_j} + F_i + \Pi \delta_{i1}, \tag{2.1a}$$

$$\frac{\partial u_i}{\partial x_i} = 0, \tag{2.1b}$$

where t is time, x_j is the coordinate vector, u_i are the velocity components, p is the pressure, ν is the kinematic viscosity, ρ is the fluid density, F_i is the penalisation forcing term, added to the momentum transport equation to enforce the no-slip/no-penetration boundary condition on a particle's boundary, and Π is the driving force term used for periodic flow simulations. Kronecker delta δ_{i1} indicates the direction of the driving force term. The penalisation forcing term (Fadlun *et al.* 2000) is calculated as

$$F_i = \frac{v_i - u_i}{\Delta t}, \tag{2.2}$$

where v_i is the velocity imposed at the boundary of the particle (i.e. zero for a stationary object) and Δt is the time step used in the simulation. Here, the index $i = 1$, 2 and 3 denotes the streamwise, spanwise and wall-normal directions, respectively, as sketched in figure 1.

The governing equations are spatially discretised using a second-order accurate, finite-difference method over a staggered grid, and integrated in time using a third-order accurate, three-step Runge–Kutta method based on the fractional-step algorithm (Kim & Moin 1985; Costa 2018; Ferziger, Perić & Street 2019). All the terms in the momentum equation are discretised explicitly and the time integration is performed such that the Courant–Friedrichs–Lewy number does not exceed a value of 0.95. The governing equations are solved using the massively parallel numerical simulation framework CaNS, which has been extensively validated for channel flows at high Reynolds numbers (Costa 2018). The computational domain is parallelised using the two-dimensional pencil domain decomposition library developed by Li & Laizet (2010) and implemented using modern Fortran (Fortran 2004) using the Message-Passing Interface (MPI) for efficient parallel communication over multiple nodes. Additional details of the computational methodology are discussed in Costa (2018) and are not repeated here for brevity.

To introduce a floating carpet composed of individual spheres, an MPI-enabled signed-distance-field (SDF) generator is used (Patil, Paranjothi & García-Sánchez 2025), which is based on a geometry-local distance algorithm. All solid objects introduced within the computational domain are identified by correctly masking the negative SDF values that correspond to the inside of the solid object. As for the initial condition, to guarantee rapid development of a turbulent boundary layer for the flow transition simulations (figure 2*f–h*), a physical obstacle is placed at the bottom wall to mimic a tripping device traditionally used in experimental facilities. For the simulations with periodic boundary conditions along the streamwise and the spanwise directions, however, a pair of vortices is introduced at the top of the channel that descend downwards to induce turbulence (Perry, Lim & Teh 1981; Wu 2023). A no-slip condition is enforced at the bottom boundary and the top (smooth and rough) boundary, and a free-slip condition is imposed for the free surface assuming the rigid-lid assumption. All data are averaged in time and along the homogeneous directions, respectively, after an initial spin-up time of 10 eddy turnovers ($T_\epsilon \equiv H/u_{*b}$, where H is the channel height and u_{*b} is the friction velocity at the smooth bottom boundary) and the results are averaged over a total of $15T_\epsilon$.
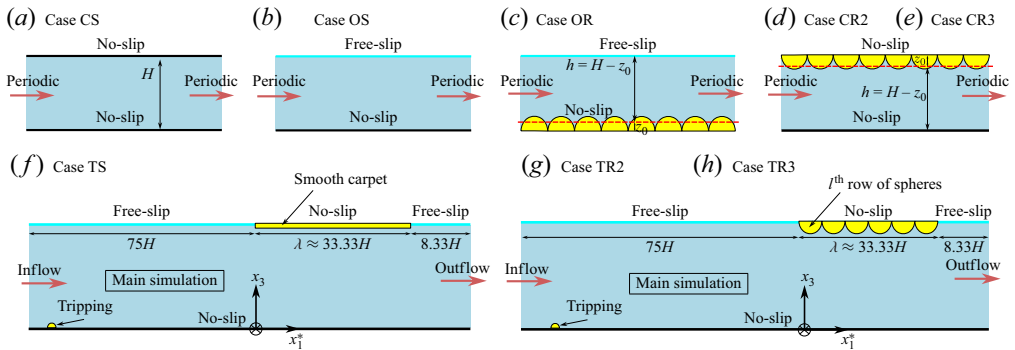
Figure 2. Various simulation scenarios considered in this work. (*a*–*e*) Periodic boundary conditions are employed with a constant bulk velocity U_{bH}, while in (*f*–*h*) inflow/outflow conditions are used with a tripping mechanism for a rapid development of the turbulent boundary layer. (*a,b,d,e*) Auxiliary simulations that are used to compare the flow development of the cases in (*f*–*h*). The latter three simulations consider the flow transition from the free-slip to no-slip condition at the top boundary. In further analysis of transition cases TS, TR2 and TR3, the $x_1^* = x_1 - 75H$ coordinate is used for streamwise direction as shown in (*f*–*h*).

In this work, the flow quantity θ is decomposed as

$$\theta(x_i, t) = \overline{\theta}(x_i) + \theta'(x_i, t) = \langle\overline{\theta}\rangle(x_3) + \widetilde{\theta}(x_i) + \theta'(x_i, t), \tag{2.3}$$

where $\overline{\theta}$ denotes the time-averaged quantity, θ' the temporal (turbulent) fluctuation, $\langle\overline{\theta}\rangle$ the time- and plane-averaged quantity and $\widetilde{\theta}$ the dispersive or spatial deviations when compared with the time-averaged quantity $\overline{\theta}$. For cases where the streamwise and spanwise directions are homogeneous, a periodic boundary condition is applied along these directions (i.e. x_1 and x_2), thus allowing for the (intrinsic) plane averaging to be performed over these two coordinate directions. For cases where a flow transition is considered, the streamwise direction x_1 is no longer considered homogeneous, and the plane average is performed only over the spanwise direction x_2. However, in the streamwise direction the spatial averaging is performed over a diameter of the spheres in such cases, although the same notation $\langle\theta\rangle$ is used. A detailed explanation of the different simulation scenarios is presented in § 2.2 and figure 2.

The total force acting on the particles is extracted by integrating the penalisation forcing term over the volume of the roughness layer. The force is in turn used to determine the friction velocity at the rough layer u_{*t} via $u_{*t} = \sqrt{\langle\overline{\tau}_t\rangle/\rho}$ (Yuan & Piomelli 2014; Rouhi *et al.* 2019), where $\langle\overline{\tau}_t\rangle$ is the time- and space-averaged wall shear stress. Alternatively, the wall shear stress can be obtained from the extrapolation of the linear shear stress profile to the bed, though this approach is not applicable to flow transition cases where the fully developed flow is not yet realised. Therefore, in such cases the shear stress $\langle\overline{\tau}_t\rangle$ acting on each row of particles within the carpet (denoted as the lth row for $l = 1, 2, 3, \dots$ in figure 2*g,h*) is calculated by dividing the horizontal component of the averaged penalisation force $\langle\overline{F}_1\rangle_l$ acting on that row by the projected area, i.e. the product of the channel width B and sphere diameter d_p.

2.2. *Simulation scenarios*

To investigate the hydrodynamics of floating carpets under various flow conditions, we consider eight flow configurations as detailed in table 1 and illustrated in figure 2. The first five cases are described as (*a*) case CS: closed channel flow with both smooth bottom

Case	Description	L/H	d_p/H	$k_{s\infty}/H$	Re_{bH}	$Re_{\tau b}$	$Re_{\tau t}$	Δx^+	Δy^+	Δz^+
CS	Closed channel with smooth walls	16.6	—	—	13080	375.83	376.73	12.5	4.18	$0.21 \rightarrow 7.44$
OS	Open channel with smooth walls	16.6	—	—	13080	689.51	—	11.5	3.83	$0.19 \rightarrow 6.82$
OR	Open channel with rough walls	12.0	0.178	0.113	2880	241.03	—	0.94	0.94	$0.94 \rightarrow 0.96$
CR2	Closed channel with small roughness	15.0	0.167	0.036	13080	312.49	701.50	7.00	3.50	$0.76 \rightarrow 4.34$
CR3	Closed channel with large roughness	15.0	0.250	0.064	13080	305.73	788.48	7.34	3.58	$0.79 \rightarrow 4.38$
TS	Flow transition to smooth top	116.67	—	—	13080	—	—	10.5	7.00	$0.76 \rightarrow 4.34$
TR2	Flow transition to small roughness top	116.67	0.167	0.036	13080	—	—	10.5	7.00	$0.76 \rightarrow 4.34$
TR3	Flow transition to large roughness top	116.67	0.250	0.064	13080	—	—	11.0	7.15	$0.61 \rightarrow 4.77$

Table 1. Numerical simulations corresponding to the illustrations in figure 2. For cases CR2 and CR3, the parameters are normalised by the friction velocity at the smooth bottom boundary u_{*b} specific to each case. For cases TR2 and TR3, however, the mesh parameters are normalised by u_{*b} from cases CR2 and CR3, respectively. In case TS, the flow parameters are normalised by u_{*b} from case CR2.

and top boundaries; (*b*) case OS: open channel flow with a smooth bottom boundary and free surface at the top; (*c*) case OR: open channel flow with a rough bottom boundary and free surface at the top; (*d*) case CR2; and (*e*) case CR3: closed channel with a rough top boundary and a smooth bottom boundary. Case CR2 has a relative roughness given by $d_p/H = 1/6$ and case CR3 has $d_p/H = 1/4$. The aforementioned five cases are intended as the benchmark cases, while case OR is considered to validate the volume penalisation methodology implemented for this study. Case OR corresponds to the F50 configuration in Chan-Braun, García-Villalba & Uhlmann (2011). As presented in Appendix A.1, the comparison between the methodology used in this work and the results in Chan-Braun *et al.* (2011) shows a good agreement, thus validating the current numerical framework. Details about the validation procedure can be found in Appendix A.1. As for cases CS, OS, CR2 and CR3, flow conditions and geometry parameters are identical to those of the laboratory experiments of Yan Toe *et al.* (2025). In cases CS, OS, CR2 and CR3, a constant pressure gradient drives the flow such that the bulk Reynolds number $Re_{bH} = 13\,080$ is achieved, where $Re_{bH} = (U_{bH}H)/\nu$, in which $U_{bH} = (1/H)\int_0^H \langle \overline{u}_1 \rangle \mathrm{d}x_3$ is the bulk velocity based on H.

To examine the impact of the transition, three main simulations are considered in this work, namely cases TS, TR2 and TR3 and illustrated in figures 2(*f*)–2(*h*), respectively. Case TS is the case with a transition from a smooth open channel to a smooth closed channel. Case TR2 denotes the scenario with a transition from a smooth open channel to a closed channel with a rough top boundary characterised by relatively small roughness ($d_p/H = 1/6$). Case TR3 considers a flow configuration similar to that of case TR2 with relatively larger roughness ($d_p/H = 1/4$). In these transition cases TS, TR2 and TR3, a uniform velocity profile is prescribed at the inlet boundary, and the flow develops towards a turbulent boundary layer due to the tripping placed at the bottom wall (see figure 2*f*–*h*). The tripping used in this study consists of a line of hemispheres of diameter $d_p = 0.01$ ($d_p/H \approx 0.08$) placed at $x_1 = 0.10$ m downstream of the inlet plane. The floating carpet is placed at a distance $x_1/H = 75$ away from the inlet boundary to allow a sufficiently long fetch for a fully developed condition. The length of the floating carpet layer λ is set to $\lambda/H = 100/3$. At the outlet boundary of the flow domain, a Neumann velocity boundary condition is prescribed, while the pressure at the outlet boundary is set to $p = 0$. It is noted that the current method of imposing a Neumann boundary condition on the streamwise velocity component, combined with the prescribed inflow, naturally imposes the net pressure difference that sustains the flow in this spatially developing channel as in the experiments, whereas this particular combination is not suitable for simulations of a zero-pressure-gradient turbulent boundary layer.

For all rough-channel cases CR2, CR3, TR2 and TR3, the roughness height k is defined as the radius of the individual spherical particles ($0.5d_p$) of the floating carpet as assumed by Wu, Christensen & Pantano (2020). Therefore, the relative roughness for cases CR2 and TR2 is $k/H = 0.0833$ and for cases CR3 and TR3 is $k/H = 0.125$. While the roughness height is known *a priori*, the equivalent sand grain roughness for large Reynolds number $k_{s\infty}$ and the virtual origin z_0 (Nikuradse 1933) are derived in Appendix A.2. For some of the cases listed in table 1, the location of the maximum streamwise velocity (U_{max}) is a length scale of interest and, therefore, a friction Reynolds number at the bottom boundary is defined as $Re_{\tau b} = u_{*b}z_m/\nu$, where z_m is the location of U_{max} normal to the wall, and a friction Reynolds number at the rough top boundary is defined as $Re_{\tau t} = u_{*t}(H - z_m)/\nu$. In all rough-channel simulations, the spheres are placed in a regular uniform arrangement.
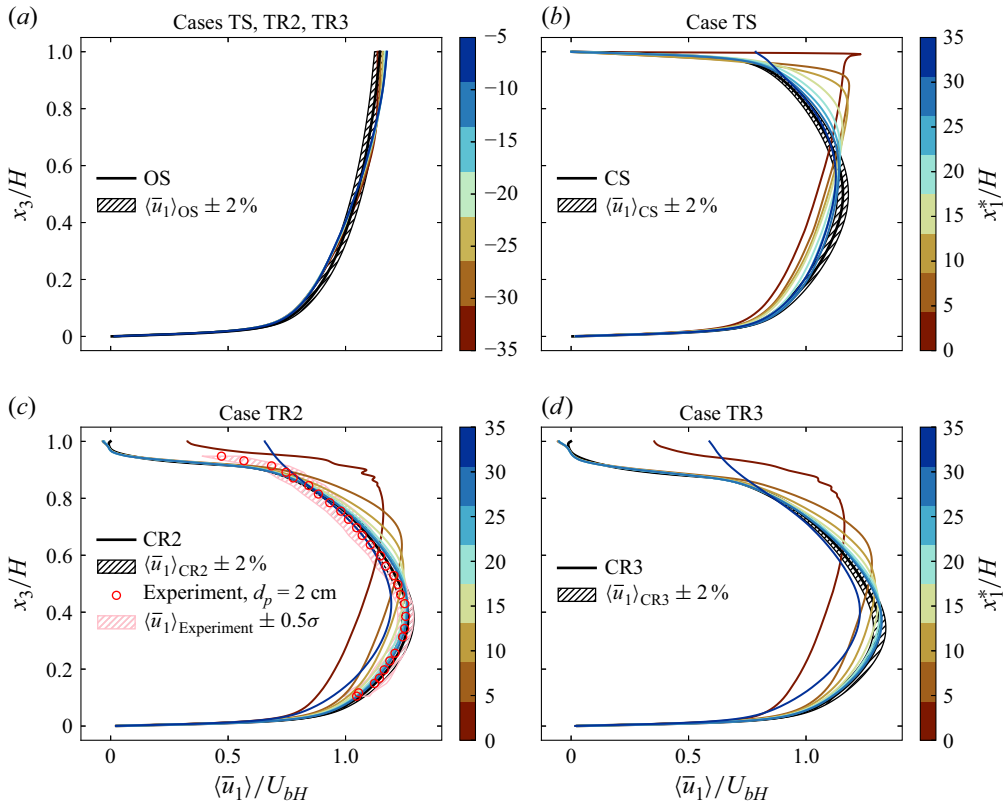
Figure 3. Mean velocity profiles (*a*) upstream of the transition for all transition cases and (*b–d*) downstream of the transition for cases TS, TR2 and TR3. The hatched area indicates $\pm 2\,\%$ of velocity profiles of cases OS, CS, CR2 and CR3, respectively. The colourbars mark the positions of the mean velocity profiles along the streamwise direction of the channel with respect to the location of the transition. The red shading in (*b*) marks $\pm \sigma/2$ around the experimental data of Yan Toe *et al.* (2025) (σ is the standard deviation). The colourbars indicate the streamwise position with respect to the transition point.

3. Results and discussion

3.1. *Streamwise development of global quantities*

To analyse the fully developed flow condition as a function of the streamwise distance from the inflow boundary, we discuss the development of the time- and plane-averaged flow parameters, i.e. mean velocity and Reynolds shear stress, for cases TR2 and TR3. These quantities are compared with the results from cases CS, OS, CR2 and CR3 that serve as benchmark datasets.

Figure 3 compares the development of time- and plane-averaged velocity profiles along the streamwise direction of the channel for cases TS, TR2 and TR3. Here the streamwise coordinate origin is set at the start of the floating carpet such that the negative values for the streamwise direction $(x_1 - 75H)/H < 0$ correspond to the flow domain upstream of the carpet, while the positive values for the streamwise direction $(x_1 - 75H)/H > 0$ correspond to the downstream reach of the carpet. Hereafter, $(x_1 - 75H)/H$ will be referred to as x_1^*/H, where $x_1^* = x_1 - 75H$, denoted by the colourbars in figure 3. The time- and plane-averaged streamwise velocity profile $\langle \overline{u}_1 \rangle (x_3)$ upstream of the transition in cases TS, TR2 and TR3 is observed to compare well with the profile obtained for the statistically stationary flow of case OS within 2 % range of accuracy (figure 3*a*). At the
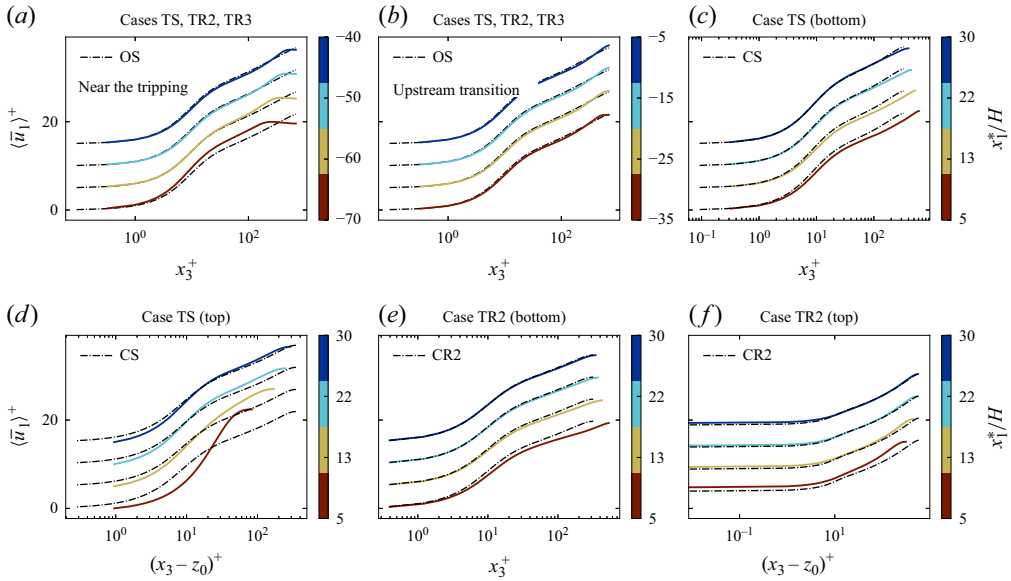
Figure 4. Comparison of mean velocity profiles normalised by inner scaling: (*a*) comparison in the vicinity of the physical tripping, (*b*) comparison upstream of the transition, (*c*) comparison in the lower half of the channel for case TS, (*d*) comparison for the upper half of the channel where the debris accumulates, (*e*) comparison for the bottom half of the channel for case TR2 after the transition and (*f*) comparison for the upper half of the channel for case TR2 after the transition. In cases TS and TR2, the velocity profiles under the carpet are divided based on the location of the maximum streamwise velocity z_m. Since velocity profiles of case TR3 do not show any significant difference from those of case TR2, results of case TR3 are omitted.

transition point $x_1^*/H = 0$ and downstream locations $x_1^*/H > 0$ as shown in figure 3(*b*–*d*), the flow encounters a floating carpet and thus undergoes an adaptation to the no-slip boundary condition. In case TS, the velocity profiles do not reach the fully developed velocity profile when compared with the benchmark profile of case CS (figure 3*b*). In contrast, case TR2 (figure 3*c*) and case TR3 (figure 3*d*) exhibit a fully developed flow condition at $x_1^*/H \approx 33$. The benchmark results from cases CS, CR2 and CR3 are also shown in figure 3(*b*–*d*).

To investigate the flow behaviour in the near-wall region, the above-mentioned velocity profiles are plotted again using the viscous length scale or wall unit in figure 4. In all subfigures, the velocity profiles are shifted by $\Delta U^+ = 5$ for clear visualisation. Figure 4(*a*) shows the evolution of the flow immediately downstream of the tripping mechanism, and the logarithmic profile is recovered at $x_1^*/H = -40$. The development of flow profiles upstream of the transition point is depicted in figure 4(*b*), showing that the approach flow to the carpet compares well against the logarithmic mean velocity profile. To study the velocity profiles in the closed channel region of cases TS and TR2, the profiles are divided based on the location of maximum streamwise velocity, and shown separately in figure 4(*c*–*f*). For the rough-channel case TR2, the velocity profiles in the top part need to be shifted for their virtual origins where the logarithmic velocity profile begins, which is further elaborated in Appendix A.2, in figure 4(*f*). The velocity profiles in all cases are observed to recover at $x_1^*/H = 30$ and agree with benchmark results. Since the velocity profiles of case TR3 show shapes similar to those of case TR2, the results of case TR3 are omitted here.

A rapid recovery of first-order statistics, i.e. mean streamwise velocity, is observed in the rough transition cases TR2 and TR3 due to the additional momentum mixing
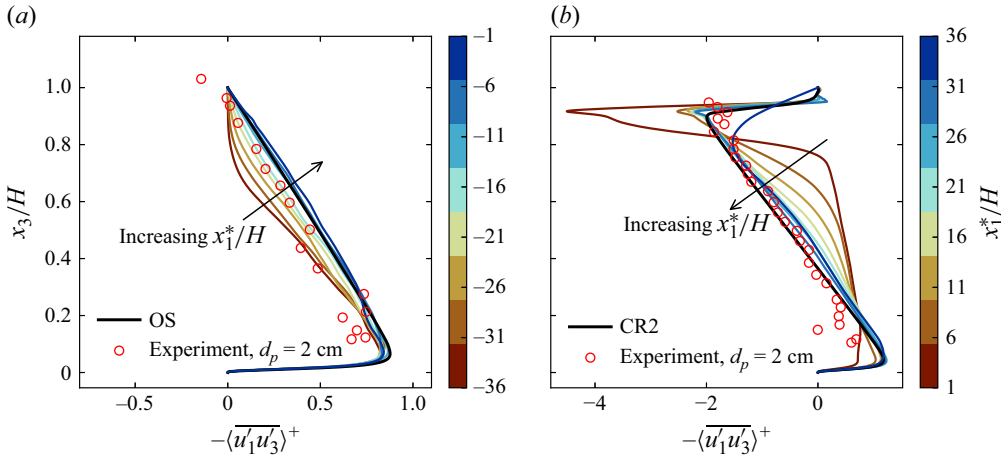
1027 A18-10

Figure 5. Reynolds shear stress profiles for case TR2: (*a*) upstream of the flow transition and (*b*) downstream of the transition. The colourbars mark the positions of the Reynolds shear stress profiles along the streamwise direction of the channel with respect to the location of the transition. Since the streamwise position $x_1^*/H \approx 36$ is beyond the end of the carpet and the flow transitions to open-channel flow again (figure 2*g*), the stress profile does not follow the benchmark profile.

induced by the spheres of the rough carpet. However, in the smooth transition case TS, the first-order statistics cannot be recovered immediately downstream of the transition. Moreover, the simulation results of cases CR2 and TR2 show a good comparison with the experimental result from Yan Toe *et al.* (2025) in the fully developed condition, except for a slight deviation near the top rough wall (figure 3*c*). It should be noted that the laboratory experiments used spheres with a slightly higher submergence of 87 %.

The streamwise evolution of the Reynolds shear stress profile for case TR2 is compared against the benchmark cases OS and CR2 in figures 5(*a*) and 5(*b*), respectively. Upstream of the transition, the Reynolds stress profiles for cases TR2 and OS are observed to be in good agreement (figure 5*a*), whereas the profiles under the carpet in figure 5(*b*) fail to recover to the linear stress profile observed for the benchmark case CR2. It is noted that at $x_1^*/H \approx -1$, which is very close to the transition point, the flow already experiences the step change and consequently the profile near the bottom boundary does not agree exactly with the benchmark velocity profile of case OS (figure 5*a*). Similarly, since the streamwise position $x_1^*/H \approx 36$ represents the location downstream of the end of the carpet, the flow transitions again to the open channel flow (denoted as free-slip boundary condition in figure 2*g*) and the stress profile is found to deviate from the benchmark case CR2 in figure 5(*b*). The relatively slow response of the Reynolds stress under the carpet follows the trends previously observed by Rouhi *et al.* (2019) and Van Buren *et al.* (2020). A similar trend was seen for case TR3, which is not shown here for brevity. There are, however, some minor differences observed closer to the bottom wall when comparing the numerical and the experimental results, which can be presumably attributed to the experimental measurement limitations and additional sidewall effects of the flume. Overall, both the time- and plane-averaged mean flow response and the Reynolds stress profile compare well with the benchmark cases, suggesting that the approach flow conditions upstream of the transition are fully developed in cases TS, TR2 and TR3. Moreover, larger shear stresses are observed near the rough top boundary compared with those near the bottom boundary downstream of the transition point because of roughness-induced turbulence stresses.
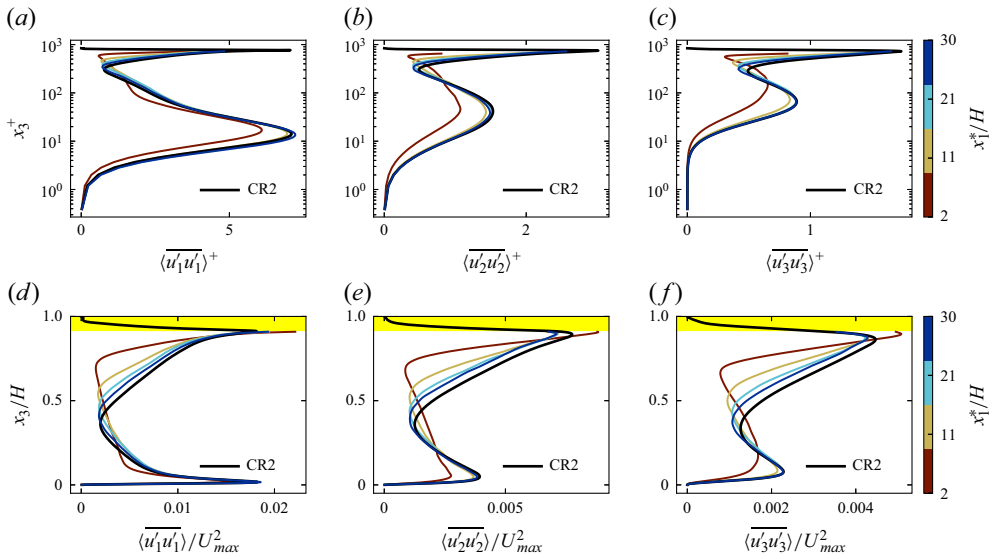
Figure 6. Vertical profiles of turbulent normal stresses $\langle \overline{u_i' u_i'} \rangle$ downstream of the transition point $x_1^*/H > 0$: (a–c) using inner scaling and (d–f) using outer scaling. Yellow-coloured areas in (d–f) indicate the height of the roughness.

It is noted that variations in debris size and shape can lead to different observations of the stress distribution.

Streamwise development of turbulent normal stresses $\langle \overline{u_i' u_i'} \rangle$ is also investigated using inner scaling and outer scaling in figures 6(a–c) and 6(d–f), respectively, for case TR2. The profiles are found to approach the benchmark results gradually as expected. As reported by Burattini *et al.* (2008), the normal stress profiles also show an asymmetric shape in the rough–smooth closed channel due to the different roughnesses. Detailed study of turbulent normal stresses is presented in Appendix A.3 for cases TS and TR3, including the development of the profiles at the inflow section, downstream of the tripping point.

To study the impact of the floating carpet on the bulk flow, we consider three different metrics that quantify the boundary-layer development: the displacement thickness (δ_*^t) given by

$$\delta_*^t = \int_0^{z_m} \left(1 - \frac{\langle \overline{u}_1 \rangle}{U_{max}} \right) dx_3, \tag{3.1}$$

the momentum thickness (Θ^t) given by

$$\Theta^t = \int_0^{z_m} \frac{\langle \overline{u}_1 \rangle}{U_{max}} \left(1 - \frac{\langle \overline{u}_1 \rangle}{U_{max}} \right) dx_3 \tag{3.2}$$

and the top boundary layer ($\delta^t \equiv z_m$) defined as the distance from the wall where the streamwise velocity has a maximum value (U_{max}). Figure 7 compares the above-mentioned metrics for the boundary-layer growth under the floating carpet for cases TS, TR2 and TR3. As the flow approaches the floating carpet, the mean flow is observed to experience the effect of the carpet even in the upstream region as indicated by δ^t (figure 7a,c,e). A more pronounced effect is observed in the case of the rough carpet (figure 7c,e), whereas a smaller effect is seen in the smooth transition case TS (figure 7a). Subsequently, the mean
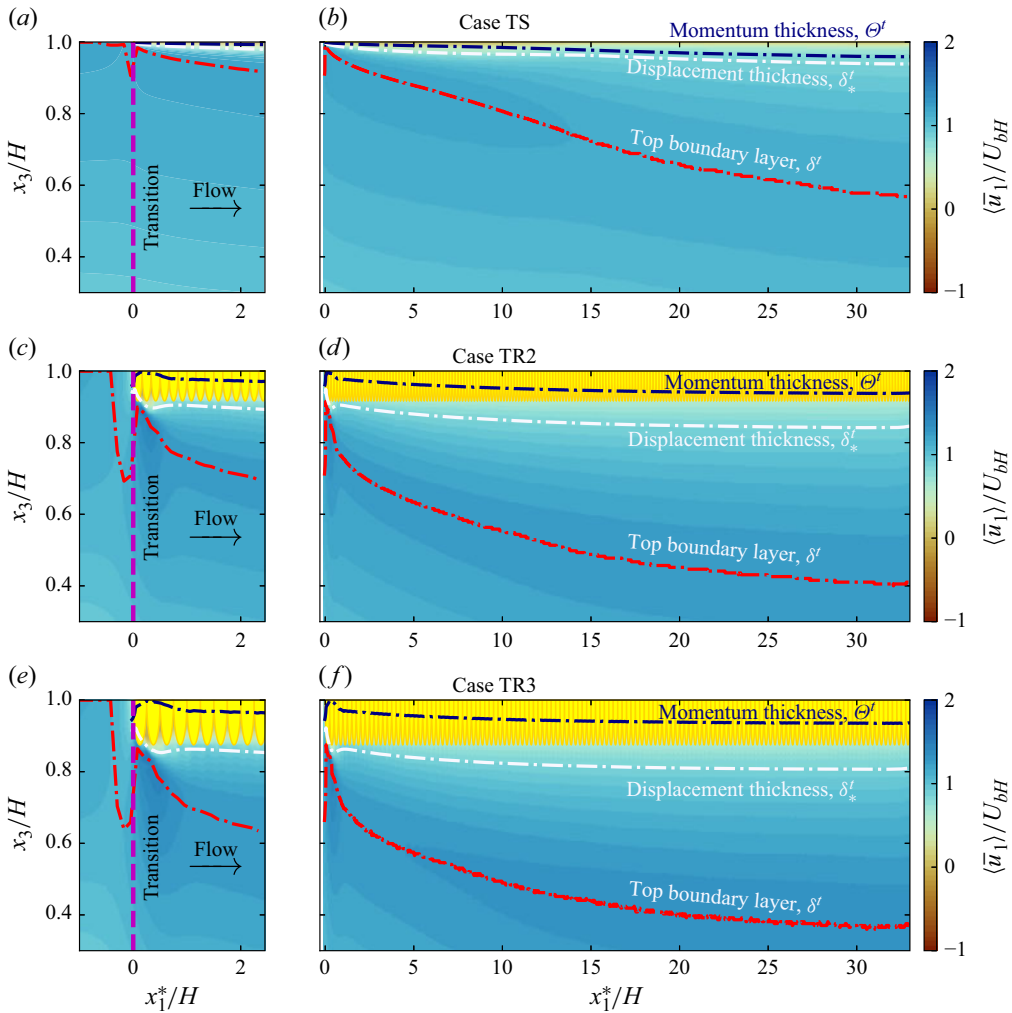
Figure 7. Development of top boundary layer δ^t, displacement thickness δ_*^t and momentum thickness Θ^t: (a,c,e) near the transition (zoom-in view for the horizontal dimension) and (b,d,f) under the carpet for cases (a,b) TS, (c,d) TR2 and (e,f) TR3. Yellow regions represent the floating carpet (not to scale).

flow deflects with a vertically downward flow as shown in figure 17. For case TR2, the top boundary layer (red dashed-dot line in figure 7d) extends from the top wall to the vertical position of $(H - \delta^t)/H \approx 0.4$ and asymptotes to a constant value along the streamwise direction at $x_1^*/H \geqslant 30$, suggesting a fully developed flow condition underneath the carpet. The momentum thickness Θ^t and the displacement thickness δ_*^t are observed to be relatively smaller compared with δ^t as expected. Comparing the boundary-layer growths across cases TS, TR2 and TR3, the relatively larger roughness height in case TR3 induces a larger boundary-layer thickness (figure 7f), while a smaller boundary layer is observed in the smooth carpet case TS (figure 7b) for all the metrics discussed above. This is especially true when comparing the asymptotic behaviour where case TR2 is observed to attain a value of $(H - \delta^t)/H \approx 0.4$, while case TS attains a smaller value of $(H - \delta^t)/H \approx 0.6$ and case TR3 attains a slightly larger value of $(H - \delta^t)/H < 0.4$
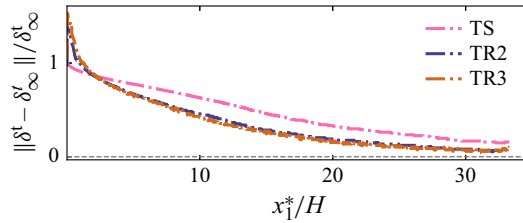
1027 A18-13

Figure 8. Relative development of top boundary layer δ^t with respect to its asymptotic value δ^t_∞. The asymptotic value is obtained from the corresponding periodic benchmark cases.

(here smaller values mean a deeper top boundary layer), thus clearly illustrating the impact of the relative roughness height.

We also quantify the relative development of δ^t with respect to the asymptotic value δ^t_∞ that is obtained from the corresponding benchmark cases, giving the ratio $\|\delta^t - \delta^t_\infty\|/\delta^t_\infty$ as shown in figure 8. All cases TS, TR2 and TR3 exhibit a similar relative growth of δ^t although the shape of case TS differs slightly from that of cases TR2 and TR3, which share an identical shape. Therefore, different roughness heights do not affect the relative growth rate of the boundary layer, $\|\delta^t - \delta^t_\infty\|/\delta^t_\infty$.

Similar to a conventional smooth boundary layer, the displacement thickness δ^{*t} and the momentum thickness Θ^t are smaller than the boundary-layer thickness δ^t in all transition cases TS, TR2 and TR3. At the location of the fully developed flow in case TR2, their ratios are found to be $\delta^t/\delta^t_* = 3.8$ and $\delta^t/\Theta^t = 9.6$, respectively. The momentum thickness is observed within the roughness layer (figure 7d), meaning that the loss of momentum in the rough boundary layer occurs mostly inside the roughness elements. In case TR3, the thicknesses of the aforementioned three layers (δ^t, δ^t_* and Θ^t) are found to be larger than those in case TR2 because the larger roughness pushes the mass and momentum mixing layers further away. Nevertheless, the ratios $\delta^t/\delta^t_* = 3.3$ and $\delta^t/\Theta^t = 9.8$ are found in case TR3, which are approximately similar to those observed in case TR2.

In addition to the study of boundary-layer thickness, we examined the internal boundary layer (IBL) δ_{IBL} and internal equilibrium layer (IEL) δ_{IEL} which show the immediate response of the flow to changes in the boundary roughness. The layer to which the effect of the new boundary roughness reaches is defined as the IBL, and the lower part of the IBL which obtains a new equilibrium with the new surface is called the IEL (Rouhi *et al.* 2019). Previous work of Rouhi *et al.* (2019) is referred to for detailed explanation and calculation method of δ_{IBL} that we apply here. In brief, the slope curve $dU^+/d \ln x_3^+$ is plotted for each x_1 position as shown in figure 9, and two successive local extrema of the slope curve are identified. Then, two linear fits are applied to the velocity profile in the semi-log scale corresponding to these extrema, and the intersection point of the two fitted lines is determined. This intersection defines the position of δ_{IBL}. Here δ_{IEL} is obtained by locating the vertical position corresponding to the first logarithmic region in a composite velocity profile consisting of several individual profiles (Savelyev & Taylor 2005). Figure 9 shows δ_{IBL} and δ_{IEL} at the rough top surface for cases TR2 and TR3. Both internal layers (δ_{IBL} and δ_{IEL}) are found to be almost identical, and inside the external top boundary layer δ^t of the rough surface as observed in the work of Rouhi *et al.* (2019). Some noise is observed in case TR2 which may be attributed to the sensitivity of the slope-finding method. The green line in figure 9 denotes a power-law fitted line, $\delta_{IBL} \propto (x_1^*)^\alpha$ as suggested by Li *et al.* (2022), for δ_{IBL} to estimate its growth rate, and it is found that δ_{IBL} varies as $(x_1^*)^{0.67}$ in case TR2 and varies as $(x_1^*)^{0.38}$ in case TR3. The observed α values lie within 0.22 and 0.886 as reported by Rouhi *et al.* (2019). It should be noted that previous studies on step
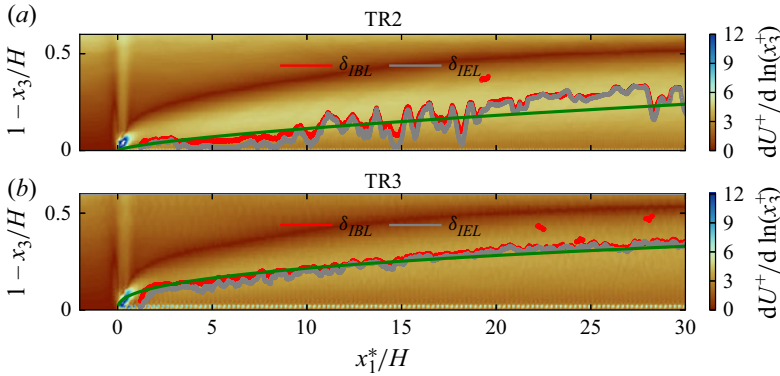
Figure 9. Internal boundary layer δ_{IBL} and internal equilibrium layer δ_{IEL} at the top rough surface for (a) case TR2 and (b) case TR3. The vertical coordinate is the inverted coordinate such that $1 - x_3/H = 0$ is the top surface. The green line is a power-law fit.
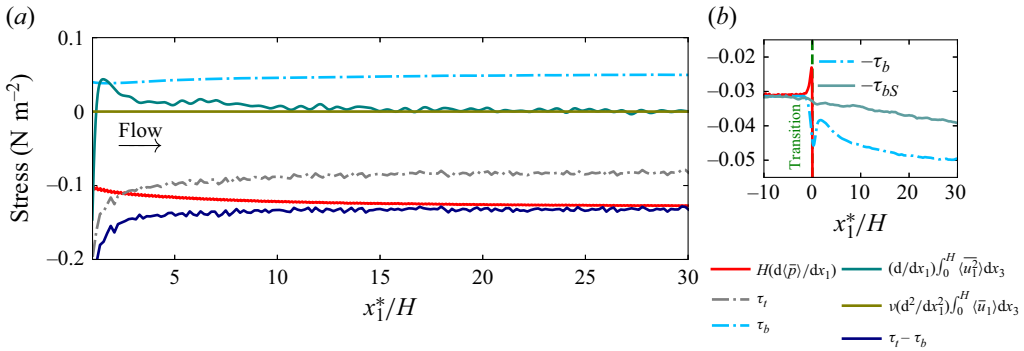

Figure 10. Different terms in the streamwise momentum balance for the fully developed flow in the closed section of case TR2. (a) Overall development along the streamwise direction after the transition and (b) change in bottom shear stress τ_b (of case TR2) and τ_{bS} (of case TS) in the vicinity of the transition. Throughout the transition region, the momentum balance is not complete without including the momentum flux term.

changes (Antonia & Luxton 1971; Li *et al.* 2019; Rouhi *et al.* 2019) did not consider the influence of the bottom boundary, but here the presence of the smooth bottom boundary is incorporated in the DNS study of rough boundary-layer development, creating a closed and asymmetric flow geometry.

Time- and spanwise-averaged momentum balance in the streamwise direction is assessed for case TR2 in figure 10 and for case TR3 in figure 11. The streamwise momentum equation for the developing flow condition can be expressed as

$$\frac{\mathrm{d}}{\mathrm{d}x_1} \int_0^H \left\langle \overline{u_1^2} \right\rangle \mathrm{d}x_3 = -\frac{1}{\rho} \frac{\mathrm{d}\langle \overline{p} \rangle}{\mathrm{d}x_1} H + \frac{\tau_t}{\rho} - \frac{\tau_b}{\rho} + \nu \frac{\mathrm{d}^2}{\mathrm{d}x_1^2} \int_0^H \langle \overline{u}_1 \rangle \, \mathrm{d}x_3, \qquad (3.3)$$

where the term on the left-hand side is the advective acceleration term, the first term on the right-hand side is the pressure gradient and the last term is the streamwise gradient of the diffusive force. For the fully developed flow, the force balance equation reads after simplification

$$\frac{\mathrm{d}\langle \overline{p} \rangle}{\mathrm{d}x_1} H = \tau_t - \tau_b \qquad (3.4)$$
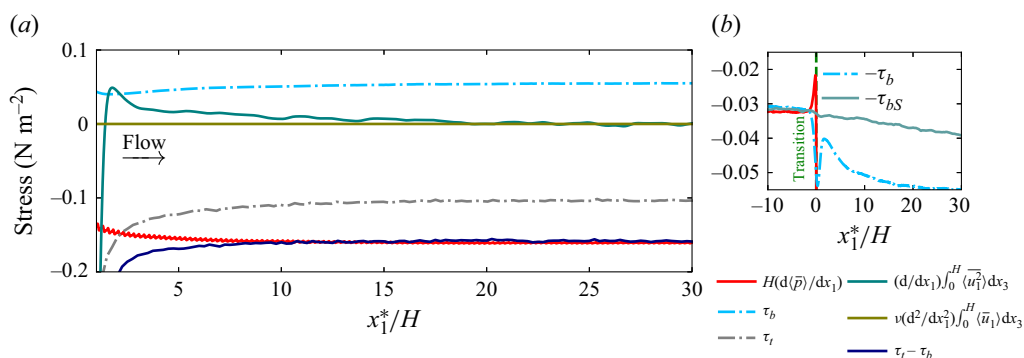
Figure 11. Same as figure 10 for case TR3. In contrast to case TR2, the flow is observed to approach the fully developed condition faster in case TR3.

implying that the pressure drop (left-hand side) is balanced by the sum of the wall shear stresses (right-hand side) at the top and the bottom walls of the closed-channel region. Here, τ_t is the stress at the top boundary and τ_b is the stress at the bottom boundary where only the viscous stress is present. For the open-channel flow upstream of the carpet, i.e. $x_1^*/H < 0$, the driving pressure gradient $\mathrm{d}\langle\overline{p}\rangle/\mathrm{d}x_1$ is balanced by the shear stress only at the bottom wall τ_b as shown in figure 10(b). In the vicinity of the transition, the momentum balance (3.4) is not valid since the flow is developing towards the new equilibrium. In this region, the local acceleration term $(\mathrm{d}/\mathrm{d}x_1) \int_0^H \langle\overline{u_1^2}\rangle\mathrm{d}x_3$ also plays an important role to balance with the pressure gradient force. Afterwards, the flow approaches the fully developed condition at $x_1^*/H \approx 30$ where the total wall shear stress $(\tau_t - \tau_b)$ is equal to the pressure gradient force. The acceleration term vanishes in the fully developed flow region as expected, and the contribution of the streamwise diffusive term $\nu(\mathrm{d}^2/\mathrm{d}x_1^2) \int_0^H \langle\overline{u_1}\rangle\mathrm{d}x_3$ is found to be insignificant (figures 10 and 11). A similar stress balance is also observed in case TR3 as shown in figure 11, however exhibiting a larger pressure drop due to the rougher surface at the top boundary. Moreover, the flow recovery is observed faster in case TR3 than in case TR2 due to additional turbulent mixing.

A remarkable increase in the bottom shear stress τ_b is noticed upstream of the rough transition in cases TR2 and TR3 around $x_1^*/H \approx 0$, compared with the bottom shear stress τ_{bS} of the smooth transition case TS as seen in figures 10(b) and 11(b). In fact, the roughness condition of the carpet (in cases TR2 and TR3) enhances the bottom shear stress by two mechanisms: (i) the additional mixing or higher Reynolds shear stress near the rough wall pushes the position of maximum velocity further towards the smooth bottom wall, thus increasing the velocity gradient near the bottom wall, and (ii) the presence of the rough top boundary increases flow blockage, which leads to a slightly higher effective bulk velocity, resulting in a higher shear stress at the bottom boundary. The second mechanism is associated with streamline convergence and flow acceleration, inducing a downward mean flow in the vicinity of the carpet. Therefore, the presence of the rough carpet, which alters the open channel flow into the closed channel, is mainly responsible for this increase in τ_b, and consequently may enhance possibly the bed erosion in the river. Such observations were reported in a study of ice-jams in a river by Luo *et al.* (2025).

The above described phenomena are also reflected in the development of the turbulent kinetic energy $(K = \langle\overline{u_i'u_i'}\rangle/2)$ shown in figure 12 for case TR2. Near the transition (figure 12a), high values of K are observed due to intense turbulent fluctuations or normal Reynolds stresses. In the closed-channel section (figure 12b), K is generally higher near
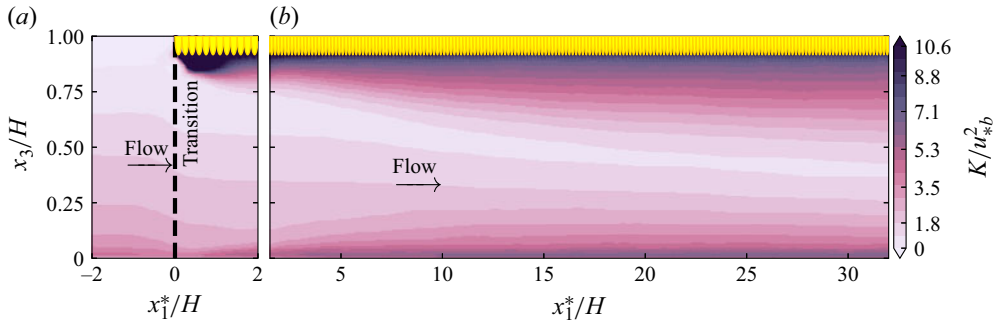
1027 A18-16

Figure 12. Turbulent kinetic energy $K = \langle \overline{u_i' u_i'} \rangle / 2$ (*a*) upstream of the transition and (*b*) downstream of the transition of case TR2, normalised by the friction velocity of smooth open-channel flow, case OS. Due to the transition, higher K level is observed not only near the top boundary but also close to the bottom boundary, which in turn enhances the mixing processes and potentially increases sediment erosion. The effect of the transition on the bottom boundary is via the convection of vortex shedding from the top shown in figure 22.

the rough top wall than near the smooth bottom wall because turbulent fluctuations are more intense due to the rough surface. The rougher top surface of case TR3 causes higher K and the smooth top surface of case TS produces a lower K level, compared with case TR2. Moreover, the roughness of the top surface promotes the K level near the bottom boundary as well, implying that, in the case of a mobile bed, more erosion can be expected.

3.2. *Skin friction*

The friction coefficient for the carpet surface C_f^t is required to estimate the cumulative shear force acting on the carpet which is responsible for the squeezing instability, as discussed by Yan Toe *et al.* (2025). Though that study assumed fully developed flow conditions along the whole carpet, the flow transition from free slip to no slip in the presence of the carpet introduces non-negligible variation of friction coefficient along the streamwise direction, affecting the accurate estimation of the compressive force. Similarly, the friction coefficient at the bottom C_f^b determines the bed shear stress and the associated turbulence level present in the water column at the transition as explained in § 3.1.

In this section, we discuss the local friction coefficients varying with the local Reynolds number $Re^* = x_1^* U_{max} / \nu$. Unlike the common definition, the local skin friction coefficient C_f is defined here as $2\tau_w / (\rho U_{max}^2)$, where τ_w denotes the wall shear stress for any type of surface and U_{max} the maximum streamwise velocity of the fully developed flow of the corresponding cases. First, simulations with periodic streamwise and spanwise boundary conditions (i.e. cases CS, OS, CR2 and CR3) provide benchmark values for the friction coefficient at the smooth bottom C_f^b and at the rough top C_f^t, indicated by the different-coloured dashed lines in figure 13. Since the flow conditions in cases CS, OS, CR2 and CR3 are fully developed flow, their friction coefficients do not vary with respect to x_1^*. Moreover, the friction coefficients of smooth surfaces are found to be identical in the fully developed flow condition, regardless of any surface type at the other side of the channel, provided that the Reynolds numbers are the same. A small difference can be expected in the comparison if the maximum velocity is slightly different and its location is slightly displaced. This is observed in our results as well in figure 13(*a*), showing that three dashed lines for C_f^b (cases CR2 and CR3) and $C_f^{t,b}$ (case CS) are almost identical.

Second, the results of simulations with flow transition (i.e. cases TS, TR2 and TR3) are shown in figure 13 with the different-coloured solid lines. Figure 13(*b*) shows the
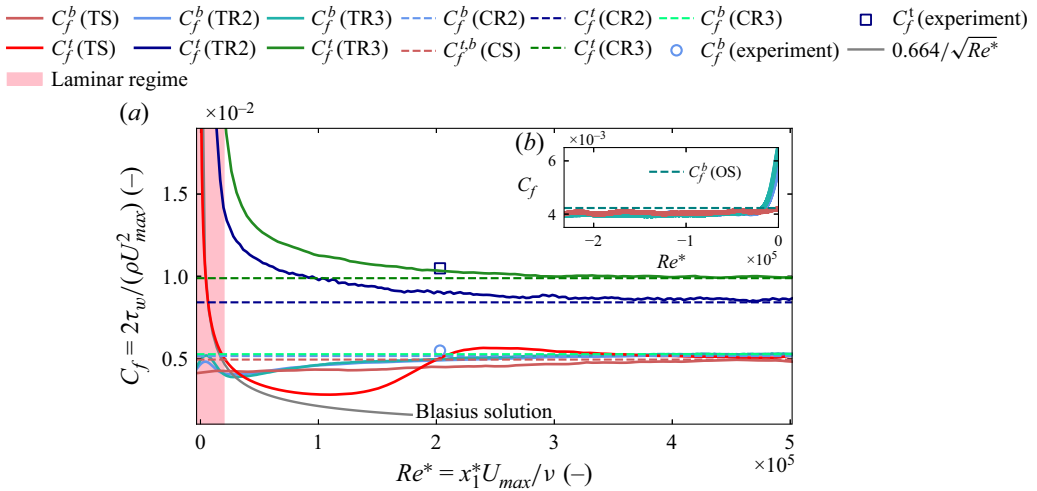
Figure 13. Friction coefficients for smooth carpet (case TS) and rough carpet (cases TR2 and TR3): (*a*) downstream of the transition and (*b*) upstream of the transition, based on the local Reynolds number Re^*. Benchmark results from simulations using periodic boundary conditions are also shown as dashed lines. It should be noted that extreme values of C_f^t (TR2) and C_f^t (TR3), which correspond to the leading edge of the carpet, are excluded here for the sake of clarity, but discussed in § 3.4.

streamwise development of bottom friction coefficient C_f^b upstream of the flow transition, i.e. the open-channel region for cases TS, TR2 and TR3. A constant friction coefficient is found until $Re^* \leqslant -0.25 \times 10^5$ where the presence of the top boundary starts to interfere with the bottom boundary layer (figure 13b). It should be noted that, since C_f^b is defined using U_{max} of the fully developed flow in the open-channel region instead of the local U_{max} within the range of $-0.25 \times 10^5 < Re^* \leqslant 0$, the increase in C_f^b is observed locally due to the accelerating flow and higher bulk velocity. This is reflected in the shear stress development as previously shown in figure 10.

Downstream development of C_f^b after the transition is shown in figure 13(*a*) for cases TS, TR2 and TR3. Adjacent to the transition, the development of C_f^b undergoes a transitional stage until it approaches the benchmark results of periodic cases CS, CR2 and CR3 at the fully developed condition ($Re^* = 5 \times 10^5$), which all provide the same C_f^b value (figure 13*a*). Compared with the value of C_f^b upstream of the transition, C_f^b is found to be larger downstream of the transition, which is also consistent with the rise of turbulent kinetic energy level K near the bottom boundary after the transition, as shown in figure 12. The experimental result of C_f^b is observed to be slightly larger than the numerical result of case TR2 at the same Reynolds number Re^* because of additional sidewalls in the experimental set-ups (figure 13). It is noted that in the laboratory experiments, C_f^b and C_f^t are indirectly estimated by a linear extrapolation of the measured Reynolds shear stress profile assuming a linear stress profile of the fully developed condition.

Now, the development of the friction coefficient at the top boundary C_f^t is studied for cases TS, TR2 and TR3. In the smooth transition case TS, the initial part of the developing C_f^t follows the Blasius solution $0.664/\sqrt{Re^*}$, followed by the transitional stage to the turbulent region as shown in figure 13(*a*). This behaviour is consistent with the observations reported by Wu & Moin (2009). Detailed comparison of current DNS results with the Blasius profile is discussed in Appendix A.4, showing the excellent agreement
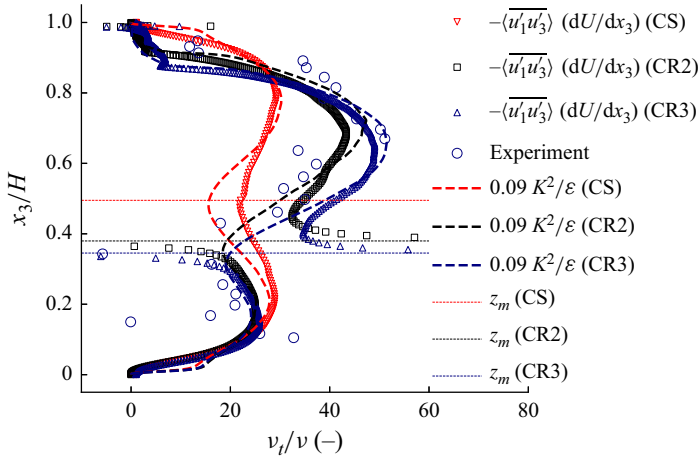
Figure 14. Eddy viscosity profiles using two different calculation approaches: (i) $v_t = -\overline{\langle u_1' u_3' \rangle}/(dU/dx_3)$ and (ii) $v_t = C_\mu K^2/\varepsilon$, where $C_\mu = 0.09$. The first approach leads to a discontinuity for asymmetric roughness cases (CR2 and CR3) while the second approach results in a continuous profile for all cases. Nevertheless, both approaches demonstrate overall similarity.

until the point of transition ($x_1^*/H \approx 1.2$ or $Re^* \approx 20 \times 10^3$) before the turbulent boundary layer. Thereafter, the friction coefficient approaches the benchmark C_f^b value of the smooth surface. Therefore, these observations collectively suggest that despite the flow transition due to the presence of the smooth carpet, the friction coefficient approaches the statistically stationary values observed for the periodic cases at the location of fully developed flow, i.e. $Re^* = 5 \times 10^5$ (figure 13a).

Similarly, in cases TR2 and TR3, the development of C_f^t follows a trend similar to that of the rough boundary-layer development as discussed earlier in figure 7. After the transition stage, their local friction coefficients C_f^t are found almost identical to the benchmark values of cases CR2 and CR3 in fully developed conditions, respectively. Having observed the development of C_f^t along the streamwise direction in case TR2, it can be concluded that C_f^t attains the fully developed value ($\simeq 8.64 \times 10^{-3}$) at $Re^* = 3 \times 10^5$. The experimental result of C_f^t is found to be larger than the simulation result of case TR2 at the same Re^* (figure 13) due to additional shear stress of the sidewalls than in the numerical simulations without the sidewalls.

3.3. *Eddy viscosity and z_m versus $z_{\tau=0}$*

This subsection discusses the eddy viscosity v_t for cases TS, TR2 and TR3, which is an indication of momentum mixing and also an important parameter for turbulence closure models such as the $k-\varepsilon$ model. The eddy viscosity v_t can be calculated using (i) the definition of Reynolds shear stress $-\overline{\langle u_1' u_3' \rangle} = v_t dU/dx_3$, where $U = \langle \overline{u_1} \rangle$, and (ii) the definition as used in the $k-\varepsilon$ model ($v_t = C_\mu K^2/\varepsilon$, where C_μ is an empirical coefficient typically taken as 0.09) using the relations $K = \langle u_i' u_i' \rangle/2$ and $\varepsilon = v \langle (\partial u_i'/\partial x_j)(\partial u_i'/\partial x_j) \rangle$ (Davidson 2015). This was shown to be valid for the log-law region of the boundary layer (Davidson 2015). It is noted that this constant 0.09 fails for the near-wall region where the turbulence is highly anisotropic, which is not considered here.

Ideally, the two aforementioned approaches should provide similar results of v_t for the region away from the wall or the middle part of the closed channel. In figure 14, which
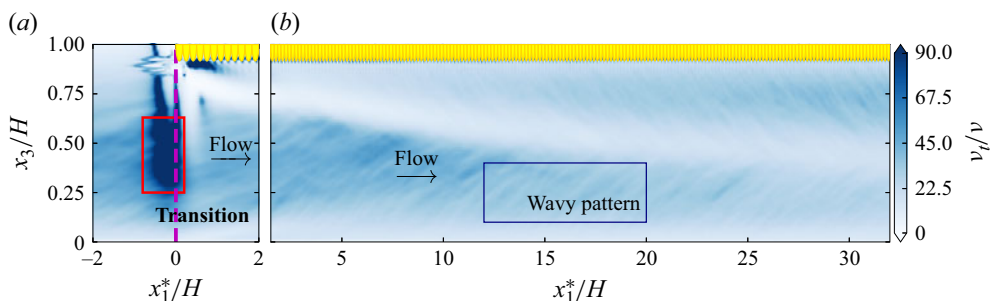
Figure 15. Development of eddy viscosity ν_t, normalised by the molecular viscosity ν, for case TR2 (*a*) upstream of the transition and (*b*) downstream of the transition. Before the transition, energetic turbulent mixing is observed in the middle part of the water column while the lower mixing zone is near the free surface due to the downward-accelerated flow. After the transition, ν_t approaches the benchmark profile shown in figure 14.

shows the ν_t profiles for cases CS, CR2 and CR3 along with experimental data, a distinct discontinuity is observed only in cases CR2 and CR3 when the first approach is used. This discontinuity is located at the position of z_m (i.e. $\mathrm{d}U/\mathrm{d}x_3 = 0$) for these two asymmetric cases, denoted by the horizontal blue and black dotted lines, respectively (figure 14). This behaviour is not observed, however, in case CS which is a simply closed smooth-channel flow, indicated by the red dotted line. Applying the second approach does not show any discontinuity in ν_t profiles for all of cases, as denoted by the dashed lines in figure 14.

Therefore, the second approach, which calculates ν_t using K and ε, is adopted in this work, as it avoids the discontinuity and shows overall good agreement with the first approach, $\nu_t = -\overline{\langle u'_1 u'_3 \rangle}/(\mathrm{d}U/\mathrm{d}x_3)$, in the outer-wall region for all cases. Figure 15 shows the streamwise development of ν_t, normalised by the molecular viscosity ν, for case TR2 using the second approach for calculating ν_t. Just upstream of the transition, a zone of high turbulent mixing is observed from $x_3/H \approx 0.25$ to $x_3/H \approx 0.65$ shown by the red rectangle in figure 15(*a*). This in turn can influence the transported material such as plastic and sediment particles. Above this energetic mixing zone, turbulent mixing decreases again because of downward-inclined accelerated flow at the leading edge of the carpet. After the flow transition, ν_t develops towards the benchmark profile, which resembles a double quadratic profile in figure 14. For case TR3, a similar behaviour is observed with the energetic mixing zone ranging from $x_3/H = 0.15$ to $x_3/H = 0.5$ (figure not shown here), which shifts downwards slightly. The wavy pattern indicated by the box in figure 15(*b*) arises from insufficient temporal averaging of the higher-order statistics used in the $k-\varepsilon$ model, without affecting the overall results here.

Figure 16 compares the vertical profiles of the viscous stress and the Reynolds shear stress for the periodic cases CS, CR2 and CR3, normalised by the total bottom shear stress ρu_{*b}^2 of the corresponding case. In case CS, the location of maximum velocity z_m coincides with the location of zero Reynolds shear stress $z_{\tau=0}$, which is a necessity resulting from the symmetry of the flow configuration (figure 16*a*). In case CR2 (figure 16*b*) and case CR3 (figure 16*c*), however, z_m is observed above $z_{\tau=0}$, i.e. the location of zero shear stress is closer to the smoother boundary compared with the location of maximum velocity. Therefore, the absolute value of shear stress is found to be large ($|\tau| > 0$) at the location of z_m, indicated by the gap in figures 16(*b*) and 16(*c*). Consequently, dividing a larger numerator by a smaller denominator leads to an extreme value and discontinuity in the ν_t profiles. Such a discrepancy between z_m and $z_{\tau=0}$ was
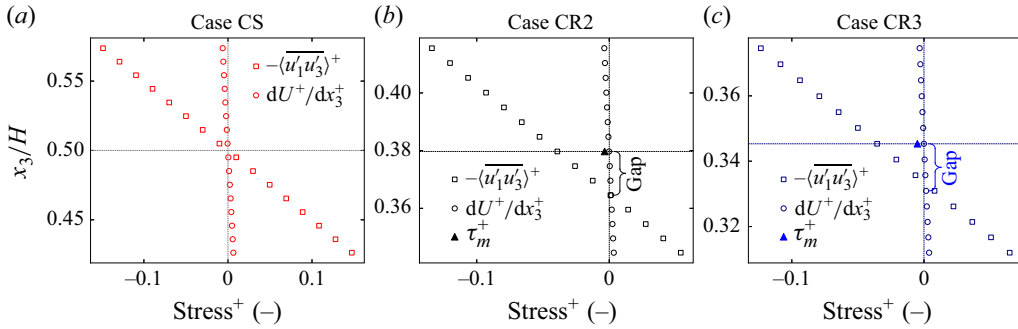
Figure 16. Shift between the position of zero Reynolds shear stress ($\tau_{13}^+ = -\langle \overline{u_1' u_3'} \rangle^+ = 0$) and the position of maximum streamwise velocity U_{max}. The analysis is performed using the data from (*a*) case CS, (*b*) case CR2 and (*c*) case CR3. The black and blue triangles denote the estimated τ_{13}^+ at the positions of U_{max} using the turbulence model of Donaldson *et al.* (1973) for case CR2 (*b*) and case CR3 (*c*), respectively.

reported in the experimental study of Hanjalić & Launder (1972), and later confirmed by Tatinclaux & Gogus (1983) who used the simple turbulence closure model of Donaldson *et al.* (1973), elaborated in Appendix A.5.

Following the model of Donaldson *et al.* (1973), the shear stress at z_m, denoted as τ_m, is estimated for cases CR2 and CR3 indicated by the filled triangle symbols in figures 16(*b*) and 16(*c*). Therefore, our numerical results for asymmetric roughness channels underpin the observation of $z_m > z_{\tau=0}$, showing a good agreement with the prediction of the turbulence model of Donaldson *et al.* (1973). However, more importantly, the fact that the location of zero shear stress does not coincide with the location of zero velocity gradient questions the validity of the eddy viscosity modelling approach in these asymmetric flows.

3.4. *Streamlines near the transition and flow separation*

When the flow approaches an obstacle or undergoes a new physical boundary, streamlines can deflect and separate based on the submergence-depth Reynolds number $Re_k = kU_{FS}/\nu$ (Fang *et al.* 2022) defined using the incoming free-stream velocity U_{FS} equivalent to the maximum velocity U_{max} in the open-channel region and submergence height which is equal to the roughness height k in our case. Using the simulation input parameters (table 1), Re_k is calculated as 1140 for case TR2 and 1925 for case TR3. For both cases, flow separation can still occur at the transition point in the lower range of Reynolds number (Tafti & Vanka 1991; Fang *et al.* 2022). In this section, we discuss flow separation and its consequence for the force on the particles near the transition.

The streamlines in the wall-normal (x_1, x_3) plane are shown for two different spanwise positions of the sphere, $x_2/d_p = 0.00$ and $x_2/d_p = 0.50$, of case TR2 in figure 17 and of case TR3 in figure 18. Here, $x_2/d_p = 0.00$ corresponds to the locations between adjacent spheres, while $x_2/d_p = 0.50$ indicates the position of the middle plane of a single sphere. To this end, the streamlines are averaged in the x_2 direction only at their corresponding x_2/d_p positions. Flow separation is observed between adjacent spheres (figures 17*a* and 18*a*) whereas streamline deflection occurs under the spheres, i.e. $x_2/d_p = 0.5$ (figures 17*b* and 18*b*). Their net effect can be obtained by averaging the streamlines over the whole spanwise direction similar to the concept of phase averaging where the phase is the spanwise position over one sphere, resulting in net flow reversal as indicated in figure 19(*b*). In case TR3, the streamlines show a stronger downward
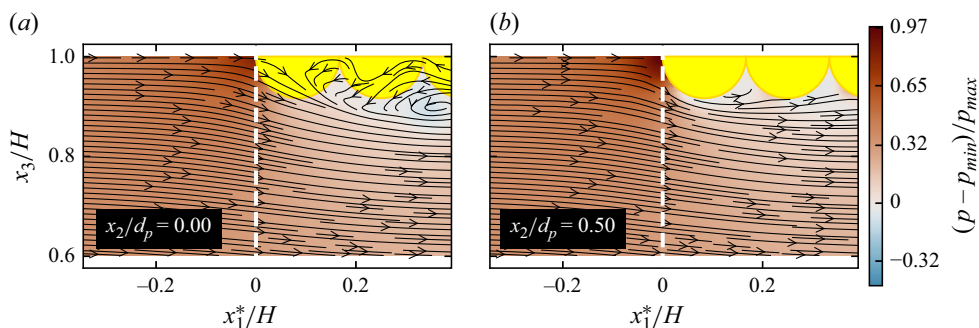
Figure 17. Streamlines near the transition for each sphere's spanwise direction (case TR2): (*a*) $x_2/d_p = 0.00$, the position between two adjacent spheres, and (*b*) $x_2/d_p = 0.50$, the middle position underneath a single sphere.
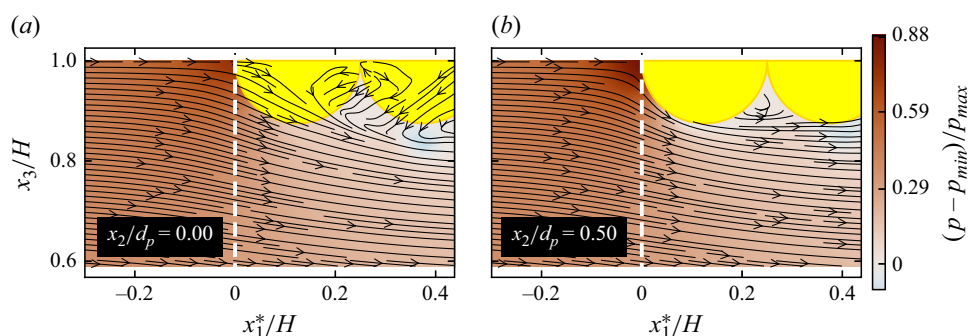

Figure 18. Same as figure 17 for case TR3. Compared with case TR2, the larger spheres in case TR3 result in a larger downward deflection of the streamlines at the transition.

deflection due to the larger roughness elements, followed by a larger flow separation zone, while the overall flow behaviour is qualitatively similar to that in case TR2. Therefore, the magnitude of streamline deflection is specific to the size of the spheres.

The net flow separation occurs within a streamwise distance of approximately $0.2 < x_1^*/H < 0.7$, which consequently affects the force direction on the spheres in the carpet. As shown in figure 19(*a*), the mean shear stress on the third and fourth rows of spheres is acting along the negative x_1 direction (i.e. upstream direction) because of the flow reversal underneath the carpet. Therefore, these particular spheres seem to be pushed in the opposite direction to the mean flow, therefore interacting with the spheres at the leading edge of the carpet which senses a force in the positive direction (i.e. downstream direction). Such a dynamic balance of forces between adjacent spheres can disturb the position of the spheres, leading to the erosion instability of the carpet. Due to the relatively large stagnation force on the leading-edge row of the spheres shown in figure 19, particle erosion occurs eventually in the positive x_1 direction.

Spanwise spatial variation due to the spheres also creates a secondary circulation between the roughness elements (Chan *et al.* 2018), leading to the formation of helical flow structures. We emphasise the flow pattern in the vicinity of the transition point, i.e. underneath the first two rows of spheres, in the spanwise plane as illustrated in figure 20 for case TR2. Each panel of figure 20 shows the $x_2 - x_3$ plane view of the streamlines
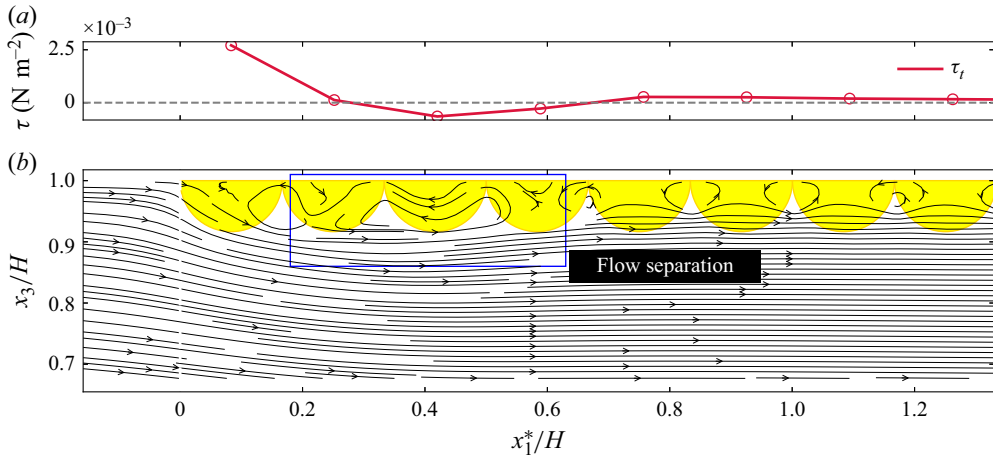
Figure 19. Flow separation under the carpet at $Re_k = 1140$ using spanwise-averaged velocity data for case TR2. (*a*) Shear stress variation along the carpet of which the third and fourth rows of spheres experience stress in the negative x_1 direction and (*b*) flow reversal under the carpet, disappearing after $x_1^*/H \approx 0.7$.
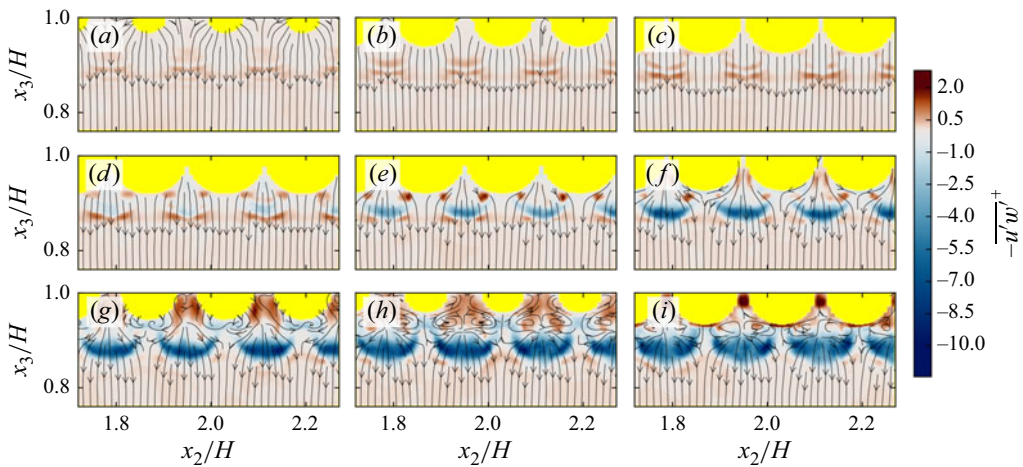

Figure 20. Streamlines near the transition point (i.e. under the first two rows of spheres) in the spanwise x_2-x_3 plane for case TR2. Each panel shows streamlines of each plane under the sphere in the increasing x_1 position. (*a–f*) The first row that experiences the strong downward-deflected flow. Nearby the second row of spheres (*g–i*), the secondary circulation is observed between the spheres, accompanied by higher turbulent shear stress.

under the sphere in the increasing streamwise x_1 position. Figure 20(*a–f*) shows the streamline pattern under the first row of spheres where the strong downward deflected flow occurs. Near the second row of spheres, secondary circulation cells are observed between the spheres as shown in figure 20(*g–i*), accompanied by higher turbulent shear stress also due to streamwise flow separation. A combination of streamwise flow separation and spanwise circulation will form a complex three-dimensional flow structure near the roughness elements.
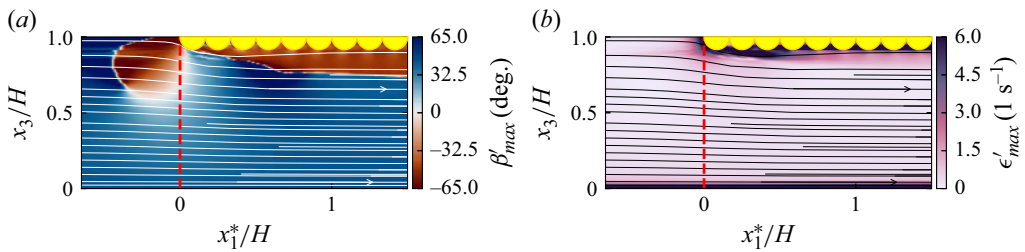
Figure 21. Principal-strain axis orientation and magnitude of maximum principal strain for CR2.

3.5. *Principal strain and vorticity*

To investigate the effect of deflected flow on the fluid deformation, an analysis of the maximum principal-strain axis β'_{max} (the direction of maximum rate of strain (Davidson 2015)) and the magnitude of strain rate ϵ'_{max} is performed for cases TR2 and TR3, assuming a two-dimensional flow problem in the wall-normal (x_1, x_3) plane. This phenomenon can cause plastic waste fibres or other pollution agents to orient with this strain axis. In general, for canonical closed-channel flow the angle β'_{max} is directed at $\pm 45°$ from the x_1 direction, showing the alignment of vortices, especially near the surface boundary. Besides, the strain rate magnitude ϵ'_{max} is strongest within the viscous sublayer or high-shear layer and is weakest in the channel centre. Strain rate ϵ'_{max} can be calculated as the largest eigenvalue of the mean strain rate tensor or using the following expression:

$$\epsilon'_{max} = \frac{\epsilon_{11} + \epsilon_{33}}{2} + \sqrt{\left(\frac{\epsilon_{11} - \epsilon_{33}}{2}\right)^2 + \epsilon_{13}^2}, \tag{3.5}$$

where $\epsilon_{11} = \partial u_1 / \partial x_1$, $\epsilon_{33} = \partial u_3 / \partial x_3$ and $\epsilon_{13} = (1/2)(\partial u_1/\partial x_3 + \partial u_3/\partial x_1)$, all averaged over time and spanwise direction. The averaging operators are dropped here for clarity. Similarly, β'_{max} can be found as the eigenvector in the $x_1 - x_3$ plane corresponding to the largest eigenvalue of the mean strain rate tensor or as follows:

$$\tan(2\beta'_{max}) = \frac{2\epsilon_{13}}{\epsilon_{11} - \epsilon_{33}}. \tag{3.6}$$

Figures 21(*a*) and 21(*b*) show the maximum principal-strain axis and its magnitude for case TR2, respectively. Due to the flow deflection at the transition point, the principal-strain axis changes from a positive direction to a negative direction near the free surface, as indicated by the brown area in figure 21(*a*). After the transition, two different principal-strain axes are observed with positive direction (blue zone) and negative direction (brown zone) near each side of the wall boundaries (figure 21*a*). This means that the maximum strain is directed in the positive direction near the bottom boundary and changes to a negative direction in the rough top boundary.

Regarding the principal strain rate magnitude ϵ'_{max} at the flow transition (figure 21*b*), its magnitude seems not very strong near the free surface, compared with in the vicinity of the bottom, though its axis direction does strongly change (figure 21*a*). Nevertheless, the strain still occurs near the free surface at the transition point because of the flow deflection.

Figure 22 shows the mean spanwise vorticity ω_2 and streamwise vorticity ω_1, both temporal- and spanwise-averaged, and normalised by u_{*b}^2/ν. At the point of flow transition, highly intense counterclockwise vortices ω_2 are observed, which can cause particle erosion at the leading edge of the carpet, as shown in figure 22(*a*). Afterwards, the intensity of ω_2 diffuses in the downstream direction while keeping its counterclockwise orientation.
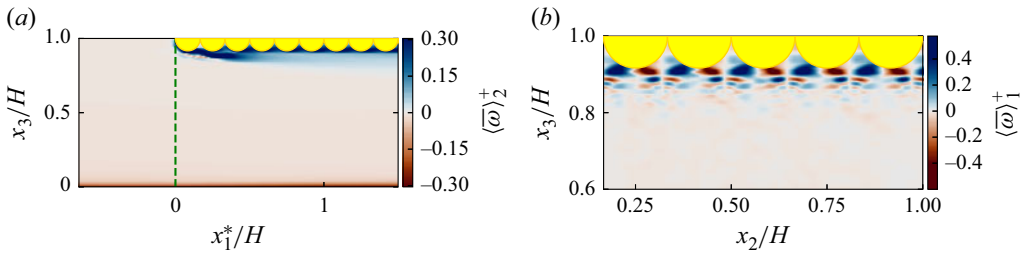
Figure 22. (*a*) Mean spanwise vorticity ω_2 and (*b*) mean streamwise vorticity ω_1, normalised by u_{*b}^2/ν, for case TR2. The top rough boundary generates strong spanwise vorticity at the transition point, which is subsequently convected towards the bottom boundary, enhancing mixing processes and potentially increasing riverbed erosion. Alternating patterns of streamwise vortices are observed around the particles near the top boundary.
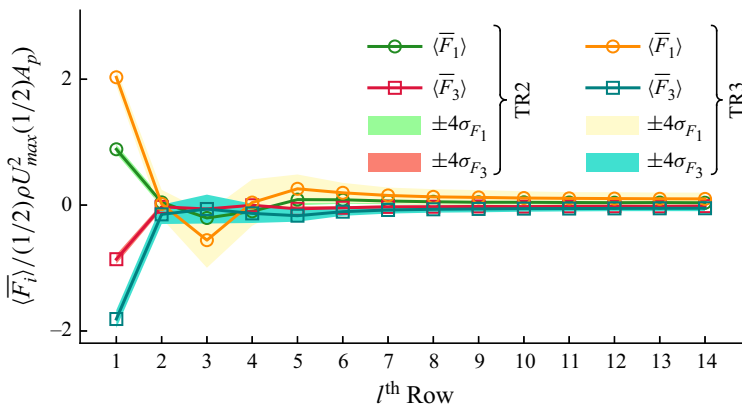

Figure 23. Mean and standard deviation of streamwise-direction and wall-normal-direction forces, F_1 and F_3, respectively, acting on each lth row of particles in the carpet for cases TR2 and TR3. The results are normalised by $(1/2)\rho U_{max}^2 (1/2) A_p$, where U_{max} is the maximum velocity of the open channel flow.

Figure 22(*b*) exhibits the streamwise vorticity ω_1 in the wall-normal (x_2, x_3) plane for the transition point. Alternating streamwise vortices are observed near the carpet layer, magnitudes of which are significantly higher than those near the bed. The regions where these alternating vortices occur are confined close to the carpet, not throughout the whole water column.

3.6. *Statistics of the forces on the particles*

Having discussed the hydrodynamics at the flow transition, we now discuss the forces acting on the spheres of the carpet. Spanwise-averaged forces acting on each lth row of the spheres $\langle F_i \rangle_l$ are discussed with their temporal-mean values and standard deviations along the carpet. Figure 23 shows the mean values of streamwise-directed force $\langle \overline{F}_1 \rangle_l$ and wall-normal-directed force $\langle \overline{F}_3 \rangle_l$ acting on each row of spheres along the carpet until the first 15 rows for cases TR2 and TR3. The mean values are obtained by averaging in time and spanwise direction. Figure 23 also shows the streamwise variation of their standard deviation values σ_{F_1} and σ_{F_3} along the carpet, multiplied by 4 for the sake of clear visualisation. The results are normalised by $(1/2)\rho U_{max}^2 (1/2) A_p$, where U_{max}

is the maximum velocity of the open-channel flow and $(1/2)A_p$ is the exposed half-area of the particle. Force fluctuation is relatively small at the first row of spheres while more important fluctuations in the hydrodynamic force are observed between the second and fifth rows, which coincide with the flow separation zone as illustrated in figure 19. Afterwards, the force fluctuations do not vary much along the carpet and are therefore omitted here for brevity (figure 23).

As reported by Yan Toe *et al.* (2025), the squeezing instability occurs to the particles inside the carpet, especially near the downstream edge or trailing edge rather than at the leading edge, because of the cumulative shear force of the upstream particles. By definition of the squeezing instability, the mean force is considered a more important contribution compared with the instantaneous force events that result from turbulent fluctuations. Moreover, significant force fluctuations are not observed after the 11th row of the particles in both cases TR2 and TR3 (figure 23). The mean force acting on the first row is found to be relatively larger than the force on the following rows of spheres in the carpet (figure 23). Therefore, the cumulative force $\langle \overline{F_1} \rangle$ acting on the particles inside the carpet can be estimated by integrating the developing force distribution along the carpet up to that particular particle's position more accurately than by just using the fully developed flow's C_f^t result as discussed in § 3.2.

In contrast to the squeezing instability, the erosion instability is triggered by a combined effect of the drag force and turbulent fluctuation forces near the transition. As shown in figure 23, the standard deviations of the forces σ_{F_1} and σ_{F_3} at the first row are not as significant as at the second, third and fourth rows where flow separation dominates. However, the mean force acting on these rows of spheres is much smaller than the mean force acting on the first row (figure 23), and therefore the first row is highly vulnerable to erosion. It should be noted that the previously discussed results are based on the spanwise-averaged force values; therefore the extreme force events are smeared out due to averaging.

Therefore, using the data collected for a single particle in the first row, we analyse the probability density function (p.d.f.) of the horizontal and vertical forces acting on it to understand the extreme force events. Figure 24(a,b) shows the p.d.f. of turbulent fluctuation forces F_1' and F_3' for cases TR2 and TR3, normalised by their standard deviations σ_{F_1} and σ_{F_3}. For both cases TR2 and TR3, the tail of the F_1' p.d.f. is right-skewed, while that of F_3' is left-skewed, compared with the Gaussian distribution. This skewness is attributed to the flow transition, where the horizontal impact force F_1' prevails in contrast to a uniform flow for which the skewness is not observed.

Though the shape of the p.d.f. is skewed, the question as to whether these extreme events can contribute to triggering the erosion instability or not, is not obvious. Indeed, particle erosion or dislodgement is determined not only by the magnitude of the force but also by whether the duration of the force is sufficient for the particle to respond. Therefore, we relate the particle's response time t_p and temporal auto-correlation functions for horizontal and vertical force components, $R_{F_1 F_1}$ and $R_{F_3 F_3}$, respectively, to investigate the temporal scale of fluid–particle interaction. The particle's response time t_p is estimated using

$$t_p = \frac{\rho_p d_p^2}{18\mu\left(1 + 0.15Re^{0.687}\right)}, \tag{3.7}$$

where ρ_p is the density of the particle (taken as 500.0 kg m^{-3}, since half of the sphere is submerged in the computational domain) and μ is the dynamic viscosity of the fluid (10^{-3} kg m^{-1} s^{-1}) (Zaidi 2018).
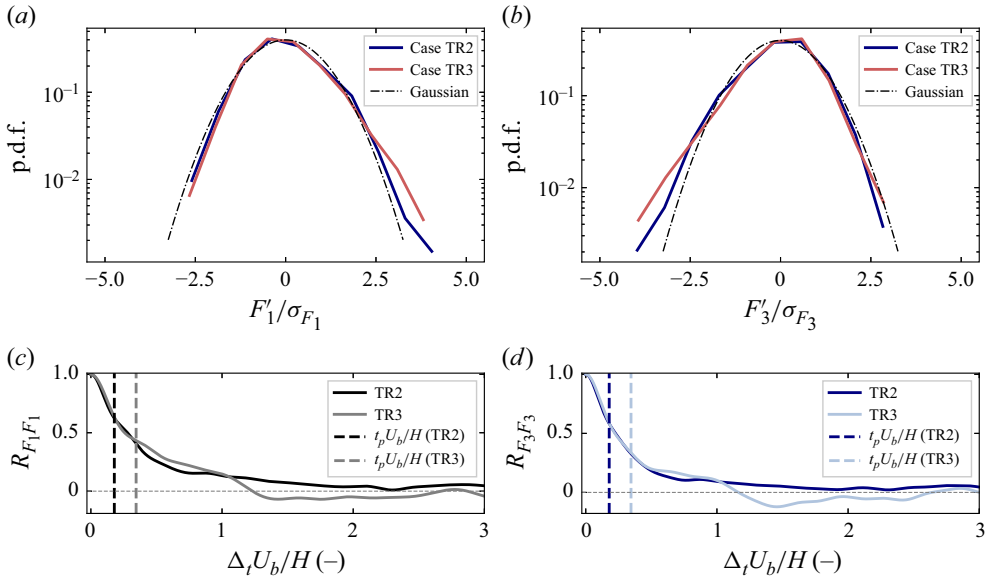
Figure 24. Normalised p.d.f. of the forces acting on a single particle in the first row of the carpet: (*a*) F_1' and (*b*) F_3' for cases TR2 and TR3; auto-correlation function (*c*) $R_{F_1 F_1}$ for F_1 and (*d*) $R_{F_3 F_3}$ for F_3 for cases TR2 and TR3. The particle response times t_p for $d_p = 2$ and 3 cm are shown using $\rho_p = 500.0 \, \text{kg m}^{-3}$.

Figure 24(*c*,*d*) shows the temporal auto-correlation functions $R_{F_1 F_1}$ and $R_{F_3 F_3}$ for cases TR2 and TR3, and the particle response times t_p are also shown for $d_p = 2$ and 3 cm. The temporal correlation of forces with durations shorter than the particle's response time (to the left of the vertical lines in figure 24) occurs on a time scale too brief to contribute significantly to particle erosion. Therefore, the force fluctuations corresponding to these time scales should be reduced accordingly in the analysis. This consideration is similar to the impulse-based criterion of Celik *et al.* (2010). Larger particles require longer duration of extreme events to erode than smaller particles (figure 24*c*,*d*), consistent with the findings of Yousefi, Costa & Brandt (2020).

While not directly shown here, figure 24(*c*,*d*) should not be interpreted to suggest that the equilibrium conditions forced in the static carpet simulation cannot occur, since the stability of the carpet relies not only on the characteristic time scale of the force but also on the impulse, i.e. force times the duration over which the force acts, that determines the stability the individual particle. Inspired by laboratory experiments of Yan Toe *et al.* (2025), the imposed bulk velocity U_{bH} in the numerical simulation is set well below the threshold velocity for particle erosion. It is therefore justified to assume that the simulated carpet remains undeformed and static during the flow development. Increasing the bulk velocity in the simulation would induce particle erosion, necessitating a dynamic particle simulation, which is computationally expensive for this particular Re_{bH} and domain size.

The downward destabilising force ($F_\downarrow$) acting on a sphere in the first row of the carpet was estimated by Yan Toe *et al.* (2025), based on the definition of erosion as the complete dislodgement of the sphere from the carpet. The reader is referred to that work for further details. Here, we briefly revisit the explanation for clarity. The downward destabilising force sketched in figure 25 is estimated as

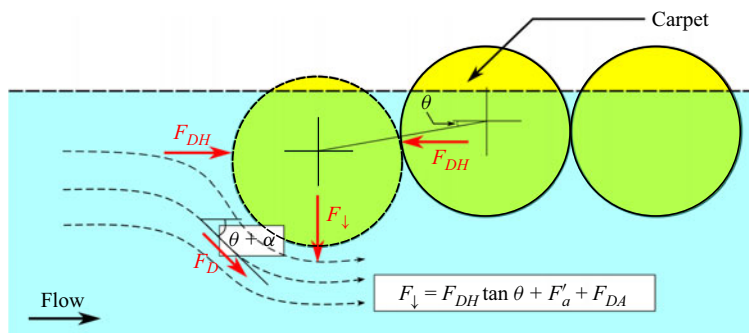$$F_\downarrow = F_{DH} \tan \theta + F_{DA} + F_a', \tag{3.8}$$

Figure 25. Sketch for force definitions in (3.8): F_D denotes fluid drag force acting along the deflected streamline, F_{DH} the horizontal component of F_D, F_{DA} the vertical component of F_D (i.e. $F_{DA} = F_D \sin(\alpha + \theta)$), F'_a the turbulent fluctuation force, α the angle of streamline deflection in the undisturbed condition where the particle does not mobilise and θ the misalignment angle between the particles (based on Yan Toe *et al.* (2025)).

where F_{DH} denotes the horizontal component of the drag force directed along the curved streamline (or the contact force with the adjacent particle), θ the misalignment angle between the centre of the eroded sphere and the undisturbed sphere, F_{DA} the downward component of the drag force of the deflected streamline, F_D, and F'_a the turbulent pressure fluctuation force emerged from the fully developed open-channel flow upstream of this point and estimated by $\rho C_f^b U_{bH}^2$, where C_f^b is the friction velocity of the open-channel flow. To estimate F_{DH} and F_{DA}, the deflection angle of the approached streamline in the undisturbed condition (α) is required and it is found to be 19° using $\arctan(\langle \overline{u} \rangle_y / \langle \overline{u} \rangle_x)$ for case TR2. In the present configuration, since the spheres are fixed in the computational domain without any vertical movement, the misalignment angle θ between two particles is zero, resulting in the destabilising force $F_\downarrow = F_{DA} + F'_a$, where $F_{DA} = F_D \sin \alpha$. The drag force acting on the particle due to the deflected streamline F_D is calculated as $0.5 \rho C_D U_{bH}^2 A_p$, where C_D denotes the drag coefficient of the sphere, taken to be 0.5 (Yan Toe *et al.* 2025).

The mean downward force for case TR2 is calculated to be 0.0003 N, which is significantly lower than the numerical simulation result of 0.0011 N. Similarly, for case TR3, the numerical simulation provides 0.0022 N while the analytical equation predicts 0.0007 N with streamline deflection angle $\alpha \approx 20°$. This discrepancy may be attributed to the lower drag coefficient of the sphere C_D assumed in the formulation of F_D. In fact, the drag coefficient needs to be accurately determined for a sphere situated in the flow transition region and packed among adjacent spheres, as this configuration significantly differs from that of an isolated sphere in a uniform flow.

4. Conclusions

This study examined the hydrodynamics associated with the transition from open-channel to closed-channel conditions, drawing motivation from practical challenges such as ice cover in rivers, plastic debris accumulation at hydraulic structures and logjams at bridges. In such scenarios, the flow undergoes a redevelopment of the boundary layer at the newly formed top surface. Simultaneously, the flow near the bottom boundary must adjust to the evolving hydrodynamic conditions induced by the transition.

To better understand the flow physics in such a transition, we employed DNS coupled with the volume penalisation technique to answer the following questions:

(i) How do the shear stresses and the friction coefficients develop along the bottom and top boundaries beyond the carpet transition?

At the transition, the bottom shear stress forms a hump-shaped profile, in contrast to the relatively uniform stress observed in the open-channel section, and gradually approaches a constant value at the fully developed flow condition of the closed-channel section. This hump-shaped shear stress profile is attributed to flow acceleration caused by the cross-sectional contraction, as well as the downward streamline deflection induced by the carpet geometry. As for the top carpet boundary, the shear stress at the transition is significantly large compared with the stress along the whole carpet, and it decreases to the constant value of the fully developed flow condition. Due to the flow separation under the carpet, especially near the transition, the shear stress opposite to the mean flow occurs there. As the shear stress is significantly large near the transition, evaluating the accurate cumulative compressive force should include the complete stress development as $\int_0^\lambda \tau_t(x_1) B \mathrm{d}x_1$, rather than just considering the constant shear stress of the fully developed condition as $\tau_t \lambda B$.

Analysis of the friction coefficients C_f^t and C_f^b for the flow transition cases shows that their developing behaviour is similar to what is observed in a developing pipe flow. Once the flow in the transition cases reaches the fully developed condition, the C_f^t and C_f^b values are also found to be similar to those in the benchmark cases.

(ii) What changes in the mean flow are observed near the transition?

Analysis of the force balance indicates that significant flow acceleration occurs at the transition because of the abrupt change in the boundary condition from free slip to no slip. In the transition region, the local acceleration force is balanced predominantly by the pressure gradient force until the flow approaches the new fully developed region. Moreover, streamlines are observed to be deflected around the leading edge of the top boundary, followed by a short region of flow separation. The streamline deflection turns the angle of the fluid's principal strain to the negative direction, even before the transition point. This means that the flow is already affected upstream of the transition. The negative principal-strain direction can cause fibre-like plastic wastes to align with it during their transport trajectory.

(iii) What are the implications for riverbed scouring and particle instability of debris accumulation? Due to the asymmetric roughnesses at the top and bottom boundaries, the location of streamwise maximum velocity z_m is found to be different from the location of zero shear stress $z_{\tau=0}$, supporting the experimental observation of Hanjalić & Launder (1972) and Tatinclaux & Gogus (1983) who observed that $z_\tau = 0$ is closer to the smooth wall than z_m. Moreover, the asymmetric roughness causes z_m and $z_{\tau=0}$ shift further towards the smoother surface. Therefore, the practical consequence of the rough top boundary can be seen in riverbed erosion under debris accumulation or ice-jams. Besides, in the above-mentioned flow separation region, the particles experience a force acting in the opposite direction to the mean flow, thus counteracting with the preceding particles experiencing a force in the mean flow direction. This leads to the particles being more vulnerable to erosion instability. Eventually, the stagnation force acting on a preceding particle is relatively larger than this opposite force; therefore the mean resultant erosive force will be in the positive x_1 direction.

Case	L/H	B/H	d_p/H	Re_{bH}	$N_1 \times N_2 \times N_3$	Extra layer	Spacing between spheres
Chan-Braun *et al.* (2011)	12.0	3.0	0.178	2880	$3072 \times 768 \times 256$	Yes	$2\Delta x$
Current method	12.0	3.0	0.178	2880	$3072 \times 768 \times 256$	No	0

Table 2. Simulation set-ups for benchmark test (from Chan-Braun *et al.* 2011) and current method (case OR). Here N_1, N_2 and N_3 denote the number of meshes in streamwise, spanwise and wall-normal directions, respectively.

Although this study employs a fixed top rough surface to model the geometric transition without incorporating significant vertical motion, the results demonstrate a good agreement with experimental observations from similar configurations. Future research should incorporate the dynamic motion of the accumulation layer, including the movement of individual particles, to more accurately capture the temporal dynamics of particle squeezing and erosion.

Appendix A

A.1. *Validation of volume penalisation method in CaNS*

To validate the volume penalisation functionality of CaNS, we performed a benchmark test using a similar set-up to that of Chan-Braun *et al.* (2011), which is an open-channel flow over a rough bed. That study included an additional sublayer under a top layer of spheres and spacing $2\Delta x$ between the spheres (Δx is the mesh spacing), whereas our simulation set-up does not consider the sublayer and the extra spacing (details in table 2).

Figures 26(*a*) and 26(*b*) show the streamwise mean velocity U shifted by the virtual origin z_0 in linear scale and in semi-log scale, respectively. In figure 26(*b*), a negligibly small deviation is observed near the rough bed, which can be due to the lack of an extra layer under the main layer in our current simulation. Similarly, a small difference is found near the bottom in the Reynolds stresses between the benchmark results and our current results as shown in figure 26(*c*). The overall good comparison between these two results validates the quality of the CaNS volume penalisation implementation.

A.2. *Determination of virtual origin and $k_{s\infty}$*

In the periodic rough–smooth channel flows (cases CR2 and CR3), the virtual origin z_0 needs to be determined to further define the effective flow depth $h = H - z_0$, the bulk velocity based on effective depth $U_{bh} = (1/h) \int_{z_0}^{H} \langle \overline{u}_1 \rangle \mathrm{d}x_3$ and the friction velocity at the
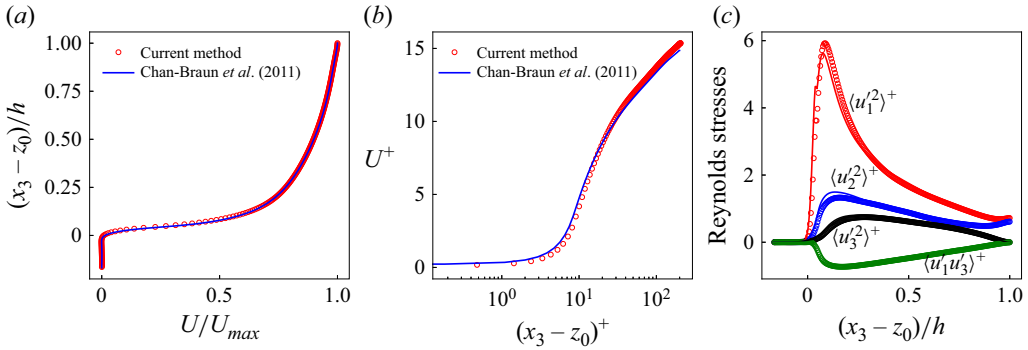
Figure 26. Validation of volume penalisation method in CaNS: (*a*) mean velocity profile in the outer unit, (*b*) mean velocity profile in the wall unit and (*c*) Reynolds stresses. Open circles indicate the current method's results while the continuous lines the benchmark test results.
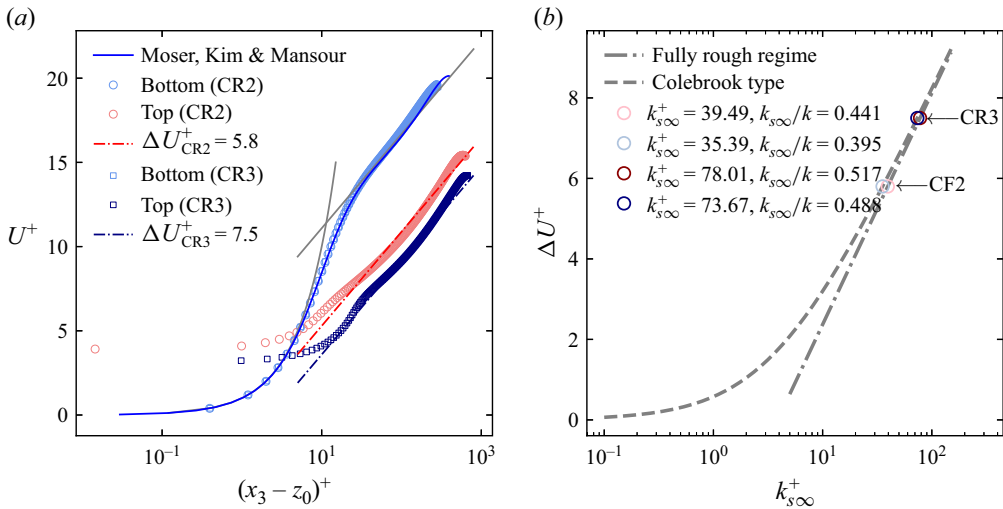

Figure 27. (*a*) Determination of virtual origin for cases CR2 and CR3 by fitting the shifted log-law profile and (*b*) estimation of equivalent sand roughness for high Reynolds number using the Colebrook formula and the fully rough regime formula.

rough wall u_{*t}. Here $\langle \overline{u}_1 \rangle$ denotes the time- and horizontal-averaged velocity profile, which is a function of only the wall-normal coordinate x_3.

For simplicity, we assume that the rough carpet lies at the origin $x_3 = 0$, and the smooth surface at the top $x_3 = 0.12$, i.e. the flipped geometry of cases CR2 and CR3. In any case, z_0 is measured from the base surface of the roughness elements, therefore assuming the flipped geometry cannot make any deviation for further analysis. Moreover, we separate the vertical extent into two parts, based on the location of maximum streamwise velocity U_{max}, and we consider only the lower part which includes the spheres.

The virtual origin is found iteratively by fitting the shifted log profile as shown in figure 27(*a*), resulting in the velocity shift ΔU. The resulting ΔU can be used to estimate the equivalent sand roughness height $k_{s\infty}$ for high Reynolds number by applying the Colebrook-type formula or fully rough regime formula (Chan-Braun *et al.* 2011). Both formulae give the conclusion for case CR2, which lies near the upper limit of the transitionally rough regime, and for case CR3, which is in the fully rough regime (figure 27*b*).
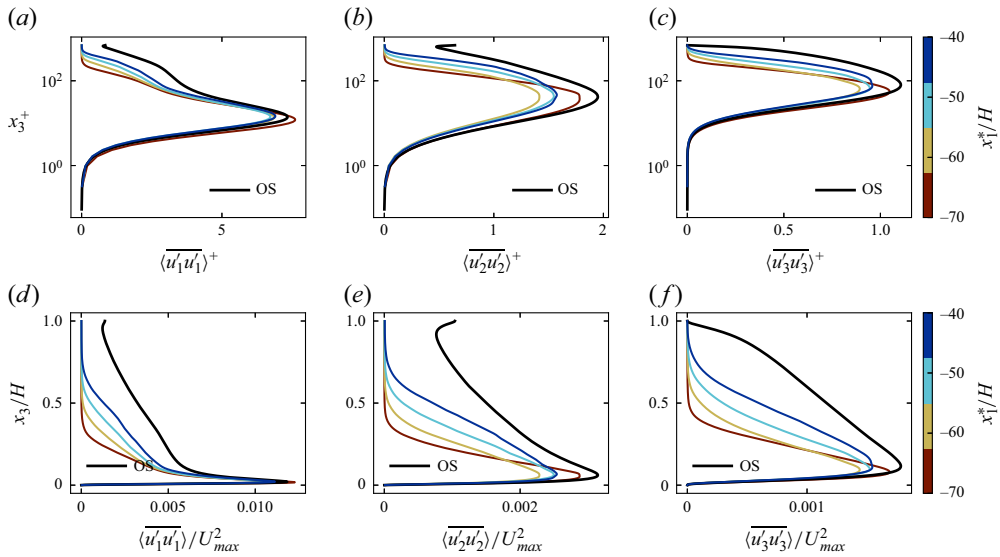
Figure 28. Streamwise development of turbulent normal stresses $\langle \overline{u_i' u_i'} \rangle$ immediately downstream of the tripping point for all transition cases TS, TR2 and TR3 using (*a–c*) the inner scaling and (*d–f*) the outer scaling. The flow is observed to be developing at $x_1^*/H = -40$.

A.3. *Streamwise development of turbulent normal stresses*

In this appendix, we address the streamwise development of turbulent normal stresses using inner scaling and outer scaling. The inner scaling is performed by the viscous length scale at the smooth boundary and the outer scaling is performed by the total depth and the maximum velocity of the corresponding case. Figure 28 illustrates the development of stress profiles immediately downstream of the tripping point and the flow is still developing at $x_1^*/H = -40$, compared with the benchmark result of case OS. However, when the flow approaches the transition point, the stress profiles attain the benchmark profiles of the canonical open-channel flow as shown in figure 29.

Figures 30 and 31 show the evolution of normal stress profiles for cases TS and TR3, respectively. The flow is found to be still evolving towards the fully developed condition in case TS whereas the flow is observed to be approaching faster the fully developed state in case TR3. The latter case induces stronger turbulent mixing due to the larger roughness.

A.4. *Validation of case TS with Blasius profile*

In case TS where a smooth carpet is introduced at the transition point, the flow encounters a hydrodynamic regime change from the open channel flow to the closed channel flow. Consequently, the flow near the free surface experiences a no-slip boundary condition of the smooth carpet, and the resulting velocity profile is found to be similar to the Blasius profile. Figure 32 compares the current DNS simulation result of the velocity profile and numerical integration result of the Blasius profile governed by

$$2\frac{\mathrm{d}^3 f}{\mathrm{d}\eta^3} + f\frac{\mathrm{d}^2 f}{\mathrm{d}\eta^2} = 0, \tag{A1}$$

where f is an unknown function of η and η denotes a transformation variable defined as $\sqrt{U/(\nu x_1)}x_3$. In figure 32, the velocity profiles are shown for the vicinity of the top boundary using the inverted vertical coordinate system $(H - x_3)$, normalised by H.
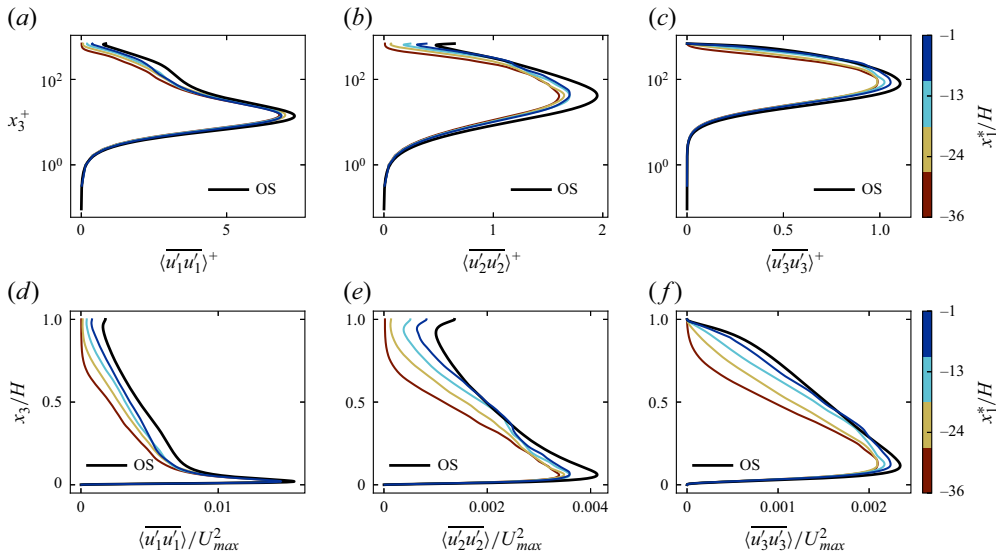
1027 A18-32

Figure 29. Streamwise development of turbulent normal stresses $\langle \overline{u_i' u_i'} \rangle$ immediately upstream of the flow transition for case TR2 using (*a–c*) the inner scaling and (*d–f*) the outer scaling. The flow is observed to follow the benchmark results of case OS in the vicinity of the transition.
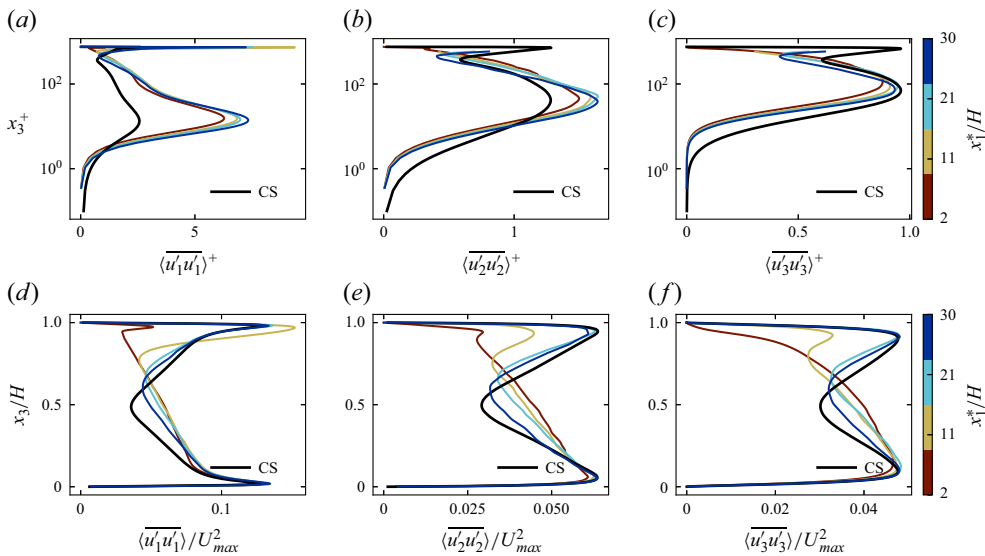

Figure 30. Streamwise development of turbulent normal stresses $\langle \overline{u_i' u_i'} \rangle$ downstream of the flow transition for case TS using (*a–c*) the inner scaling and (*d–f*) the outer scaling. The flow does not fully recover towards the benchmark closed-channel case.

Development of the velocity profiles along the streamwise position x_1^*/H is shown in the subfigures of figure 32 and they are observed to agree with the laminar boundary layer of the Blasius profile. This observation was also reflected in the discussion of C_f^t in § 3.2, showing that the new boundary layer developed at the smooth transition point is similar to the laminar boundary layer until the streamwise position of $x_1^*/H = 1.2$.
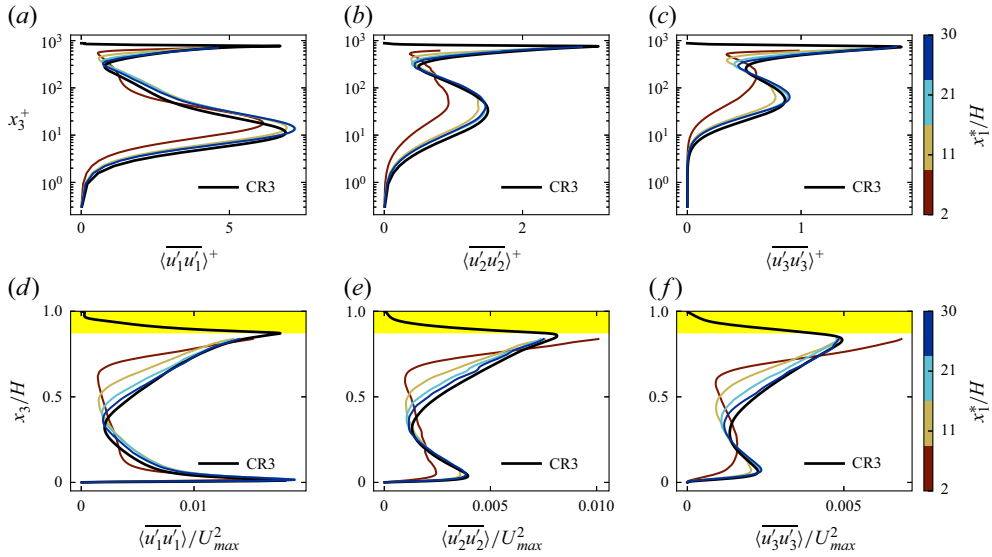
Figure 31. Streamwise development of turbulent normal stresses $\langle \overline{u_i' u_i'} \rangle$ downstream of the flow transition for case TR3 using (a–c) the inner scaling and (d–f) the outer scaling. The flow recovers the profiles of benchmark case CR3 at $x_1^*/H = 30$. The yellow-coloured area indicates the height of the roughness.
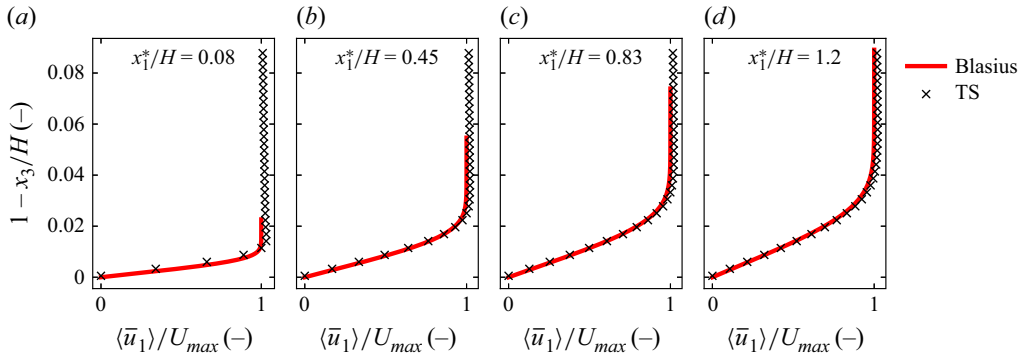

Figure 32. Comparison of mean streamwise velocity profile of case TS near the top boundary in the vicinity of the transition point ($x_1^*/H = 0.58$) against the Blasius profile. The velocity profile is shown using the inverted vertical coordinate ($H - x_3$), normalised by H, such that $1 - x_3/H = 0$ denotes the origin of the top boundary.

A.5. *Turbulence model of Donaldson et al. (1973)*

A simplified version of turbulence model developed by Donaldson *et al.* (1973) is presented briefly to estimate the shear stress at the location of streamwise maximum velocity, z_m. The transport equation of the Reynolds shear stress $\overline{u_1' u_3'}$ is the starting point of this turbulence model:

$$
\frac{\mathrm{D}\overline{u_1' u_3'}}{\mathrm{D}t} = -\overline{u_3' u_3'} \frac{\partial U}{\partial x_3} + 2\Lambda_2 \frac{\partial}{\partial x_3} \left(K \frac{\partial \overline{u_1' u_3'}}{\partial x_3} \right) + \Lambda_3 \frac{\partial}{\partial x_3} \left(K \frac{\partial \overline{u_3' u_1'}}{\partial x_3} \right) - \frac{K}{\Lambda_1} \overline{u_1' u_3'}
$$

$$
+ \nu \frac{\partial^2 \overline{u_1' u_3'}}{\partial x_3^2} - 2\nu \frac{\overline{u_1' u_3'}}{\Lambda_4^2}, \tag{A2}
$$

where Λ_i $(i = 1, \ldots, 4)$ denote the length scales to be estimated. For steady flow (which is similar to our periodic simulation cases CR2 and CR3), the left-hand side of (A2) becomes zero. The shear stress at the location of maximum velocity z_m can be calculated from the following equation:

$$0 = \left[(2\Lambda_2 + \Lambda_3) \frac{\partial K}{\partial x_3} \frac{\partial \overline{u_1' u_3'}}{\partial x_3} - \frac{K}{\Lambda_1} \overline{u_1' u_3'} - 2\nu \frac{\overline{u_1' u_3'}}{\Lambda_4^2} \right]_{z_m}, \qquad (A3a)$$

$$\tau_m = -\rho \overline{u_1' u_3'} \Big|_{z_m} = \left[-\rho \frac{2\Lambda_2 + \Lambda_3}{c} \frac{\partial K}{\partial x_3} \frac{\partial \overline{u_1' u_3'}}{\partial x_3} \right]_{z_m}, \qquad (A3b)$$

where $c = K/\Lambda_1 + 2\nu/\Lambda_4^2$, since the velocity gradient $\partial U/\partial x_3$ is zero, the viscous stress is negligible at z_m and the second derivative of the linear stress function is zero.

The model parameters of Λ_i $(i = 1, \ldots, 4)$ for application to boundary layers are as follows: $\Lambda_1 = 0.15\delta_{0.99}$, $\Lambda_2 = 0.1\Lambda_1$, $\Lambda_3 = 0.1\Lambda_1$, $\Lambda_4 = \Lambda_1/(2.5 + 0.125Re_{\Lambda_1})^{0.5}$, where $\delta_{0.99}$ is the thickness of the layer in which the velocity reaches 99 % of free-stream velocity and $Re_{\Lambda_1} = K\Lambda_1/\nu$ (Donaldson *et al.* 1973). It is noted that these parameters were derived for the atmospheric boundary layer. Therefore, we applied $\delta_{0.99} = H$, the total depth in our case.

Moreover, we can deduce the mismatch between the location of zero shear stress $z_{\tau=0}$ and the location of maximum velocity z_m by observing the signs of each term in (A3) according to Tatinclaux & Gogus (1983). The constant term $\rho(2\Lambda_2 + \Lambda_3)/c$ is positive by definition, and the gradient terms $\partial K/\partial x_3$ and $\partial \overline{u_1' u_3'}/\partial x_3$ are also found to be positive in the location of maximum velocity z_m. Therefore, the value of τ_m becomes negative (non-zero) and, consequently, $z_{\tau=0}$ is lower than z_m.

REFERENCES

ANTONIA, R. A. & LUXTON, R. E. 1971 The response of a turbulent boundary layer to a step change in surface roughness part 1. Smooth to rough. *J. Fluid Mech.* **48** (4), 721–761.

BELTAOS, S. 1983 River ice jams: theory, case studies, and applications. *J. Hydraul. Eng.* **109** (10), 1338–1359.

BURATTINI, P., LEONARDI, S., ORLANDI, P. & ANTONIA, R. A. 2008 Comparison between experiments and direct numerical simulations in a channel flow with roughness on one wall. *J. Fluid Mech.* **600**, 403–426.

CELIK, A. O., DIPLAS, P., DANCEY, C. L. & VALYRAKIS, M. 2010 Impulse and particle dislodgement under turbulent flow conditions. *Phys. Fluids* **22** (4), 046601.

CHAN, L., MACDONALD, M., CHUNG, D., HUTCHINS, N. & OOI, A. 2018 Secondary motion in turbulent pipe flow with three-dimensional roughness. *J. Fluid Mech.* **854**, 5–33.

CHAN-BRAUN, C., GARCÍA-VILLALBA, M. & UHLMANN, M. 2011 Force and torque acting on particles in a transitionally rough open-channel flow. *J. Fluid Mech.* **684**, 441–474.

COSTA, P. 2018 A fft-based finite-difference solver for massively-parallel direct numerical simulations of turbulent flows. *Comput. Math. Appl.* **76** (8), 1853–1862.

DAVIDSON, P. 2015 *Turbulence: An Introduction for Scientists and Engineers*. Oxford University Press.

DONALDSON, C.D., *et al.* 1973 Construction of a dynamic model of the production of atmospheric turbulence and the dispersal of atmospheric pollutants. In *Workshop on Micrometeorology*, vol. 313, p. 392. American Meteorological Society.

FADLUN, E. A., VERZICCO, R., ORLANDI, P. & MOHD-YUSOF, J. 2000 Combined immersed-boundary finite-difference methods for three-dimensional complex flow simulations. *J. Comput. Phys.* **161** (1), 35–60.

FANG, X., TACHIE, M. F. & DOW, K. 2022 Turbulent separations beneath semi-submerged bluff bodies with smooth and rough undersurfaces. *J. Fluid Mech.* **947**, A19.

FERZIGER, J. H., PERIĆ, M. & STREET, R. L. 2019 *Computational Methods for Fluid Dynamics*. Springer.

Fortran 2004 Fortran 2003, ISO/IEC 1539-1:2004 - Information technology - Programming languages - Fortran - Part 1: base language (Fortran 2003). International Organization for Standardization & International Electrotechnical Commission. Available at: https://wg5-fortran.org/f2003.html.

GUO, J., SHAN, H., XU, H., BAI, Y. & ZHANG, J. 2017 Exact solution for asymmetric turbulent channel flow with applications in ice-covered rivers. *J. Hydraul. Eng.* **143** (10), 04017041.

HANJALIĆ, K. & LAUNDER, B. E. 1972 Fully developed asymmetric flow in a plane channel. *J. Fluid Mech.* **51** (2), 301–335.

HUAI, W., CHEN, H., YANG, Z., LI, D. & WANG, F. 2024 Estimation of the suspended sediment concentration in ice-covered channels based on the gravitational theory. *J. Hydrol.* **637**, 131337.

ISMAIL, U., ZAKI, T. A. & DURBIN, P. A. 2018 Simulations of rib-roughened rough-to-smooth turbulent channel flows. *J. Fluid Mech.* **843**, 419–449.

JUEYI, S., JUN, W., YUN, H. E. & FAYE, K. 2010 Velocity profiles and incipient motion of frazil particles under ice cover. *Intl J. Sediment Res.* **25** (1), 39–51.

KIM, J. & MOIN, P. 1985 Application of a fractional-step method to incompressible navier–stokes equations. *J. Comput. Phys.* **59** (2), 308–323.

LI, M., DE SILVA, C. M., CHUNG, D., PULLIN, D. I., MARUSIC, I. & HUTCHINS, N. 2022 Modelling the downstream development of a turbulent boundary layer following a step change of roughness. *J. Fluid Mech.* **949**, A7.

LI, M., DE SILVA, C. M., ROUHI, A., BAIDYA, R., CHUNG, D., MARUSIC, I. & HUTCHINS, N. 2019 Recovery of wall-shear stress to equilibrium flow conditions after a rough-to-smooth step change in turbulent boundary layers. *J. Fluid Mech.* **872**, 472–491.

LI, N. & LAIZET, S. 2010 2decomp & fft-a highly scalable 2d decomposition library and fft interface. In *Cray User Group 2010 Conference*, pp. 1–13.

LUO, H., JI, H., CHEN, Z., LIU, B., XUE, Z. & LI, Z. 2025 An analytical study for predicting incipient motion velocity of sediments under ice cover. *Sci. Rep-UK* **15** (1), 1912.

NIKURADSE, J. 1933 Stromungsgesetze in rauhen Rohren. VDI-Forschungsheft 361. Laws of flow in rough pipes (in English). *NACA Tech. Memo.* 1292.

PARTHASARATHY, R. N. & MUSTE, M. 1994 Velocity measurements in asymmetric turbulent channel flows. *J. Hydraul. Eng.* **120** (9), 1000–1020.

PATIL, A., PARANJOTHI, U. C. K. & GARCÍA-SÁNCHEZ, C. 2025 Gensdf: an mpi-fortran based signed-distance-field generator for computational fluid dynamics applications. *SoftwareX* **30**, 102117.

PERRY, A. E., LIM, T. T. & TEH, E. W. 1981 A visual study of turbulent spots. *J. Fluid Mech.* **104**, 387–405.

ROUHI, A., CHUNG, D. & HUTCHINS, N. 2019 Direct numerical simulation of open-channel flow over smooth-to-rough and rough-to-smooth step changes. *J. Fluid Mech.* **866**, 450–486.

SAITO, N. & PULLIN, D. I. 2014 Large eddy simulation of smooth–rough–smooth transitions in turbulent channel flows. *Int. J. Heat Mass Trans.* **78**, 707–720.

SAVELYEV, S. A. & TAYLOR, P. A. 2005 Internal boundary layers: I. Height formulae for neutral and diabatic flows. *Boundary-Layer. Meteorol.* **115** (1), 1–25.

SCHALKO, I., SCHMOCKER, L., WEITBRECHT, V. & BOES, R. M. 2018 Backwater rise due to large wood accumulations. *J. Hydraul. Eng.* **144** (9), 04018056.

SHEN, H. T. 2010 Mathematical modeling of river ice processes. *Cold Reg. Sci. Technol.* **62** (1), 3–13.

SHEN, H. T. & HARDEN, T. O. 1978 The effect of ice cover on vertical transfer in stream channels 1. *JAWRA J. Am. Water Resour. Assoc.* **14** (6), 1429–1439.

SHEN, H. T., LIU, L. & CHEN, Y. 2001 River ice dynamics and ice jam modeling. In *UTAM Symposium on Scaling Laws in Ice Mechanics and Ice Dynamics: Proceedings of the IUTAM Symposium held in Fairbanks, Alaska, USA, 13–16 June 2000*, pp. 349–362. Springer.

TAFTI, D. K. & VANKA, S. P. 1991 A numerical study of flow separation and reattachment on a blunt plate. *Phys. Fluids A: Fluid Dyn.* **3** (7), 1749–1759.

TATINCLAUX, J.-C. & GOGUS, M. 1983 Asymmetric plane flow with application to ice jams. *J. Hydraul. Eng.* **109** (11), 1540–1554.

TORDESILLAS, A. & MUTHUSWAMY, M. 2009 On the modeling of confined buckling of force chains. *J. Mech. Phys. Solids* **57** (4), 706–727.

VAN BUREN, T., FLORYAN, D., DING, L., HELLSTRÖM, L. H. O. & SMITS, A. J. 2020 Turbulent pipe flow response to a step change in surface roughness. *J. Fluid Mech.* **904**, A38.

WU, X. 2023 New insights into turbulent spots. *Annu. Rev. Fluid Mech.* **55** (1), 45–75.

WU, S., CHRISTENSEN, K. T. & PANTANO, C. 2020 A study of wall shear stress in turbulent channel flow with hemispherical roughness. *J. Fluid Mech.* **885**, A16.

WU, X. & MOIN, P. 2009 Direct numerical simulation of turbulence in a nominally zero-pressure-gradient flat-plate boundary layer. *J. Fluid Mech.* **630**, 5–41.

YAN TOE, C., UIJTTEWAAL, W. & WÜTHRICH, D. 2025 Stability of an idealized floating carpet of plastic spheres in an open channel flow. *J. Hydraul. Eng.* **151** (4), 04025010.

YOUSEFI, A., COSTA, P. & BRANDT, L. 2020 Single sediment dynamics in turbulent flow over a porous bed–insights from interface-resolved simulations. *J. Fluid Mech.* **893**, A24.

YUAN, J. & PIOMELLI, U. 2014 Roughness effects on the reynolds stress budgets in near-wall turbulence. *J. Fluid Mech.* **760**, R1.

ZAIDI, A. A. 2018 Particle resolved direct numerical simulation of free settling particles for the study of effects of momentum response time on drag force. *Powder Technol.* **335**, 222–234.

ZUFELT, J. E. & ETTEMA, R. 2000 Fully coupled model of ice-jam dynamics. *J. Cold Reg. Eng.* **14** (1), 24–41.